submitted to *Geophys. J. Int.*

The computation of seismic normal modes with rotation as a quadratic eigenvalue problem

Jia Shi[1], Ruipeng Li[2], Yuanzhe Xi[3], Yousef Saad[4] and Maarten V. de Hoop[5]

[1] *Department of Earth, Environmental and Planetary Sciences, Rice University, USA. Email:* `jia.shi@rice.edu`

[2] *Center for Applied Scientific Computing, Lawrence Livermore National Laboratory, Livermore, CA, USA*

[3] *Department of Mathematics, Emory University, Atlanta, GA, USA*

[4] *Department of Computer Science and Engineering, University of Minnesota, MN, USA*

[5] *Simons Chair in Computational and Applied Mathematics and Earth Science, Rice University, Houston, TX, USA*

SUMMARY

A new approach is presented to compute the seismic normal modes of a fully heterogeneous, rotating planet. Special care is taken to separate out the essential spectrum in the presence of a liquid outer core. The relevant elastic-gravitational system of equations, including the Coriolis force, is subjected to a mixed finite-element method, while self gravitation is accounted for with the fast multipole method (FMM). To solve the resulting quadratic eigenvalue problem (QEP), the approach utilizes extended Lanczos vectors forming a subspace computed in a non-rotating planet – with the shape of boundaries of a rotating planet and accounting for the centrifugal potential – to reduce the dimension of the original problem significantly. The subspace is guaranteed being contained in the space of functions to which the seismic normal modes belong. The reduced system can further be solved with a standard eigensolver. The computational accuracy is illustrated using all the modes with relative small meshes, and also tested against standard perturbation calculations relative to a standard Earth model. The algorithm and code is used to compute the point spectra of eigenfrequencies in several Mars models studying the effects of heterogeneity on a large range of scales.

1 INTRODUCTION

Planetary normal modes are instrumental for studying the dynamic response to sources including earthquakes along faults and meteorite impacts as well as tidal forces (Dahlen & Tromp 1998; Lognonné 2005). For a review of Earth's free oscillations, we refer to Woodhouse & Deuss (2007). The low-lying eigenfrequencies contain critical information about the planet's large-scale structure and provide constraints on heterogeneity in composition, temperature, and anisotropy. Rotation constrains the shapes and possible density distributions of planets. The effect of rotation on the point spectrum is well understood and has been observed for decades (Park et al. 2005, Fig.1).

Early studies of normal modes of a rotating, elliptical Earth utilized Rayleigh's principle to approximate the associated eigenfrequencies (Backus & Gilbert 1961; Dahlen 1968). Later, perturbation theory (Dahlen & Sailor 1979) was developed and utilized the eigenfunctions of a spherically symmetric Earth model to estimate first- and second-order Coriolis splitting, splitting due to rotation and ellipticity (Dahlen & Tromp 1998, Chapter 14.2 and Appendix D.4). Spectral perturbation theory initially was based on self-coupling or group-coupling approaches, while later full-mode coupling scheme have been considered (Dahlen 1968, 1969; Woodhouse & Dahlen 1978; Woodhouse 1980; Park 1986; Park & Gilbert 1986; Park 1990; Romanowicz 1987; Lognonné & Romanowicz 1990; Hara et al. 1991, 1993; Um et al. 1991; Lognonné 1991; Deuss & Woodhouse 2001, 2004; Al-Attar et al. 2012; Yang & Tromp 2015). The issue with these coupling approaches is that the basis used does not lie in the space of normal modes of a rotating planet which is important, in particular, in the presence of a liquid outer core.

In our previous work (Shi et al. 2019), we separated the essential spectrum and introduce the mixed finite-element method for fully heterogeneous non-rotating planets. In a separate paper (Shi et al. 2018), we introduced a highly parallel algorithm for solving the resulting generalized eigenvalue problem using a polynomial filtering Lanczos method (Li et al. 2016). Here, we extend our previous work and include rotation in the elastic-gravitational system through the Coriolis force as well as the centrifugal potential with the appropriate constraints on the shapes of the (fluid-solid) boundaries. We utilize extended Lanczos vectors computed in a non-rotating planet – with the shapes of boundaries of a rotating planet and accounting for the centrifugal potential – as a truncated basis to reduce one of the equivalent linear forms of the quadratic eigenvalue problem (QEP). The normal modes computed are guaranteed lying in the appropriate space of functions. The reduced system can be solved with a standard eigensolver. The proposed method is accurate as we demonstrate in our computational experiments using a full mode expansion in relatively small models. We also test our computations against standard perturbation calculations relative to a standard Earth model.

We apply our algorithm and code to studying Mars models through point spectra of eigenfrequencies. This is motivated by the InSight (Interior exploration using Seismic Investigations, Geodesy and Heat Transport) (Banerdt et al. 2013; Lognonné et al. 2019) mission to Mars. It is expected that a set of eigenfrequencies is observable (Panning et al. 2017; Bissig et al. 2018). Here, we select one Mars model (Khan et al. 2016) from the set of blind tests (Clinton et al. 2017; van Driel et al. 2019) and combine it with the topography (Zuber et al. 1992; Smith et al. 1999) and a three-dimensional crust (Belleguic et al. 2005; Goossens et al. 2017) to create a realistic Mars model. We compute the low-lying eigenfrequencies and study the general effects of rotation and heterogeneity combined.

The outline of this paper is as follows. In Section 2, we revisit the form and physics of the elastic-gravitational system of a rotating planet and establish the weak formulation of the system with a separation of the essential spectrum. In Section 3, we discuss the hydrostatic equilibrium of a rotating liquid outer core in the presence of the gravitational and the centrifugal forces. In Section 4, we develop the matrix form of the resulting QEP and review various approaches to solve it. We then introduce our subspace method to reduce the dimension of the equivalent linear form of the QEP using extended Lanczos vectors. In Section 5, we illustrate the computational accuracy of our proposed method. We also show several computational experiments for different planetary models, including standard Earth and Mars models. In Section 6, we discuss the significance of our results.

2 THE ELASTIC-GRAVITATIONAL SYSTEM WITH ROTATION

In this section, we briefly discuss the weak formulation associated with the elastic-gravitational system of a rotating planet. In Subsection 2.1, we revisit the basic equations in the strong form. In Subsection 2.2, we illustrate the rotation and the centrifugal acceleration of a Mars model. In Subsection 2.3, we present the weak formulation to compute the normal modes associated with the seismic point spectrum.

2.1 The basic equations

Given the reference density ρ^0 and the gravitational constant G, we let Φ^0 denote the gravitational potential which satisfies,,

$$\Delta\Phi^0 = 4\pi G\rho^0, \tag{1}$$

and $S(u)$ denote the Eulerian perturbation of the Newtonian potential associated with the displacement, u,

$$\Delta S(u) = -4\pi G\nabla\cdot(\rho^0 u). \tag{2}$$

To include the centrifugal force, we let ψ to be the centrifugal potential

$$\psi(x) = -\frac{1}{2}\left[\Omega^2 x^2 - (\Omega\cdot x)^2\right], \tag{3}$$

where $\Omega \in \mathbb{R}^3$ is the angular velocity of rotation. We form the geopotential and its gradient,

$$g' = -\nabla(\Phi^0 + \psi). \tag{4}$$

Under the hydrostatic assumption,

$$\omega^2\rho^0 u - 2\,\mathrm{i}\,\omega\rho^0 R_\Omega u = -\nabla\cdot(c\colon\nabla u) - \nabla(\rho^0 u\cdot g') + \nabla\cdot(\rho^0 u)g' + \rho^0\nabla S(u), \tag{5}$$

where ω denotes the angular frequency and c denotes the elastic stiffness tensor; $R_\Omega u = \Omega\times u$. The boundary conditions for the system (5) governing a hydrostatic planet are shown in (Dahlen & Tromp 1998, Table 3.4).

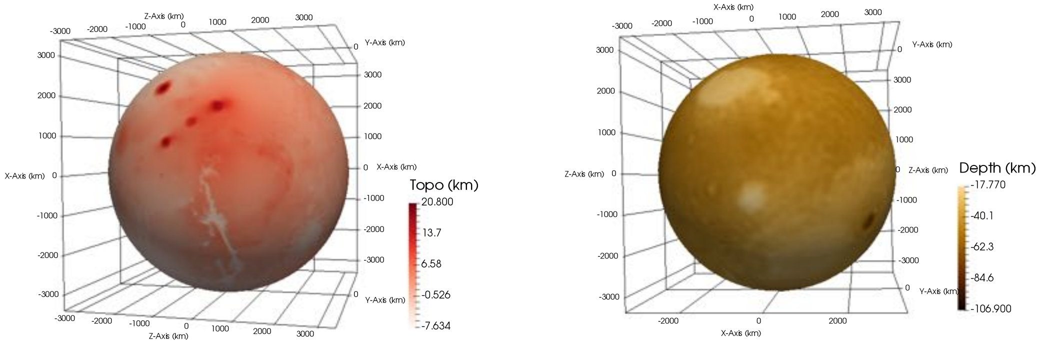

(a) Topography (b) Crust-mantle interface

Figure 1. Illustration of (a) the topography and (b) the crust-mantle interface of the Mars using MOLA and gravity data (Zuber et al. 1992; Smith et al. 1999; Goossens et al. 2017).

2.2 Illustration of the geometry and physics using a Mars model

We utilize a flexible, fully unstructured tetrahedral mesh to model multiple complicated discontinuities associated with different geological and geodynamical features. The major discontinuities are discretized using triangulated surfaces that are generated via `distmesh` (Persson & Strang 2004). We then build up the planetary model using an unstructured tetrahedral mesh via `TetGen` (Si 2015). Here, we use a Mars model as an example to illustrate our construction of a terrestrial planet. The topography of Mars was measured by the Mars Orbiter Laser Altimeter (MOLA) (Zuber et al. 1992; Smith et al. 1999) with high accuracy. The thickness and density of the Martian crust from the topography and gravity data were constrained by works of Belleguic et al. (2005); Goossens et al. (2017). In Fig. 1 (a), we illustrate the topography of Mars using data from MOLA (Smith et al. 1999); in Fig. 1 (b), we show the crust-mantle interface of Mars using data provided by Goossens et al. (2017). In Figs. 2 (a)–(c), we illustrate V_P, V_S and ρ^0 of Mars integrating a radial model (Khan et al. 2016) with a three-dimensional crust as shown in Fig. 1. In Figs. 3 (a)

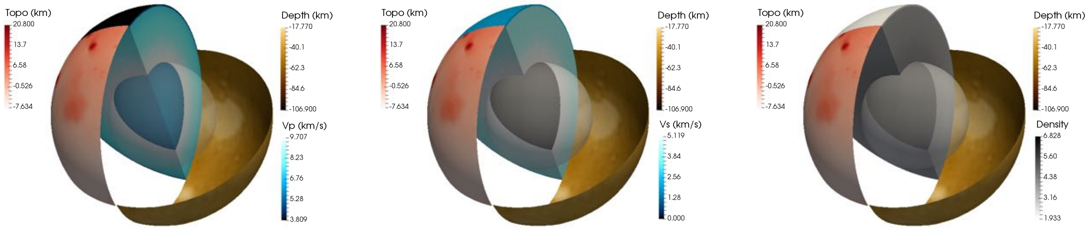

(a) V_P (b) V_S (c) ρ^0

Figure 2. Illustration of (a) V_P, (b) V_S, and (c) ρ^0 of our Mars model with a three-dimensional crust shown in Fig. 1.

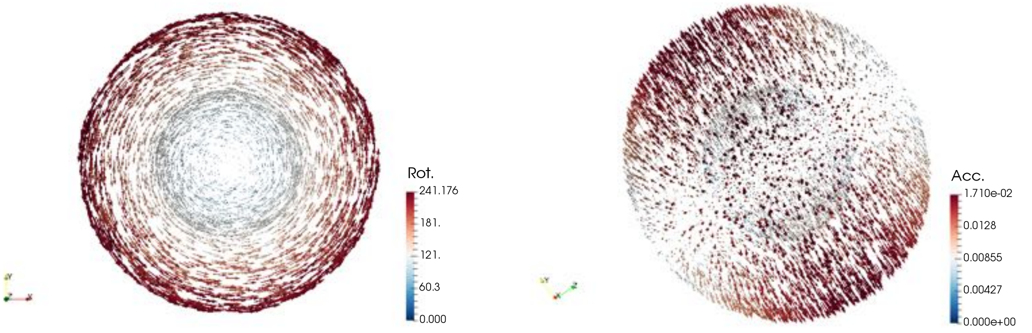

(a) The axial spin mode, $\Omega \times x$ (m/s) (b) Centrifugal acceleration, $-\nabla\psi$ (m/s^2)

Figure 3. Illustration of (a) the axial spin mode, $\Omega \times x$, and (b) the centrifugal acceleration, $-\nabla\psi$, of the Mars model shown in Fig. 2.

and (b), we illustrate the axial spin mode, $\Omega \times x$, and the centrifugal acceleration, $-\nabla\psi$, of the Mars model, respectively.

2.3 The weak formulation

Since we study a general planet with non-smooth coefficients, it is natural to utilize the weak form of the relevant system of equations. Following the notation in de Hoop et al. (2015), a bounded set $\tilde{X} \subset \mathbb{R}^3$ is used to represent the interior of the planet, with Lipschitz continuous exterior boundary $\partial\tilde{X}$. The exterior boundary $\partial\tilde{X}$ contains fluid (ocean) surfaces $\partial\tilde{X}^{\mathrm{F}}$ and solid surfaces $\partial\tilde{X}^{\mathrm{S}}$. We subdivide the set $\tilde{X}$ into solid regions Ω^{S} and fluid regions Ω^{F}. We use Σ to represent the interfaces between these subregions. In summary,

$$\tilde{X} = \Omega^{\mathrm{S}} \cup \Omega^{\mathrm{F}} \cup \Sigma \cup \partial\tilde{X},\ \partial\tilde{X} = \partial\tilde{X}^{\mathrm{S}} \cup \partial\tilde{X}^{\mathrm{F}}.$$

The interior interfaces can further be subdivided into three categories: interfaces between two fluid regions Σ^{FF}, interfaces between two solid regions Σ^{SS}, and interfaces between fluid and solid regions Σ^{FS}. This regions, interfaces and boundaries are illustrated in (Shi et al. 2019, Subsection 2.1).

In (de Hoop et al. 2019; Shi et al. 2019), we discuss the decomposition of the function space, $H = L^2(\tilde{X}, \rho^0\, \mathrm{d}x)$ into components H_1 and H_2, that is,

$$H = H_1 \oplus H_2. \tag{6}$$

We let u^s and u^f be the displacements in the solid and fluid regions, respectively, and enforce that u^f lies in H_1 by augmenting the system of equations and introducing an additional variable, p, according to

$$-\,p\kappa^{-1} = \nabla\cdot u^f + \rho^0\kappa^{-1} g'\cdot u^f \text{ in } \Omega^{\mathrm{F}}. \tag{7}$$

Here, κ signifies *the compressibility of the fluid*. Imposing the fluid-solid boundary condition $\left[\nu^{f\to s}\cdot u^f - \nu^{f\to s}\cdot u^s\right]\big|_{\Sigma^{\mathrm{FS}}} = 0$, we obtain the weak form for (7),

$$\begin{aligned}0 &= -\int_{\Omega^{\mathrm{F}}} \overline{v}^p p\kappa^{-1}\,\mathrm{d}x + \int_{\Omega^{\mathrm{F}}}\left[(\nabla v^p)\cdot u^f - \overline{v}^p(g'\cdot u^f)\rho^0\kappa^{-1}\right]\mathrm{d}x - \int_{\Sigma^{\mathrm{FS}}} \overline{v}^p(\nu^{f\to s}\cdot u^s)\,\mathrm{d}\Sigma\\ &=: c_g([u,p],v^p)\end{aligned} \tag{8}$$

for all the test functions v^p with $v^p|_{\partial\tilde{X}^{\mathrm{F}}} = 0$, where $\nu^{f\to s}$ denotes the normal vector at the fluid-solid boundary pointing from the fluid to the solid side. The same short-hand notation, $c_g([u,p],v^p)$ in (8) was introduced in (Shi et al. 2019, (16)).

For the weak formulation, we let v^s and v^f be the test functions for the displacement fields in the solid and fluid regions, Ω^{S} and Ω^{F}, respectively. To restrict the system to the computational domain, we obtain the complete formula for the rotating hydrostatic planetary model

$$\begin{aligned}a_2([u,p,S(u)],v) &= \int_{\Omega^{\mathrm{S}}} (\nabla\overline{v}^s)\colon (c\colon \nabla u^s)\,\mathrm{d}x + \int_{\Sigma^{\mathrm{FS}}} \mathfrak{S}\{(\overline{v}^s\cdot g')(\nu^{s\to f}\cdot u^s)[\rho^0]^f\}\,\mathrm{d}\Sigma\\ &+ \int_{\Sigma^{\mathrm{FS}}} (\overline{v}^s\cdot\nu^{s\to f})p\,\mathrm{d}\Sigma + \int_{\Omega^{\mathrm{S}}} \mathfrak{S}\{(\nabla\overline{v}^s)(g'\cdot u^s)\rho^0 - u^s\cdot(\nabla g')\cdot\overline{v}^s_j\rho^0 - u^s\cdot(\nabla\overline{v}^s)\cdot g'\rho^0\}\,\mathrm{d}x\\ &- \int_{\Omega^{\mathrm{S}}} [\nabla\cdot(\rho^0\overline{v}^s)]S(u)\,\mathrm{d}x - \int_{\Sigma^{\mathrm{SS}}\cup\partial\tilde{X}^{\mathrm{S}}} (\nu\cdot\overline{v}^s)S(u)[\rho^0]^{+}_{-}\,\mathrm{d}\Sigma - \int_{\Sigma^{\mathrm{FS}}} (\nu^{f\to s}\cdot\overline{v}^s)S(u)[\rho^0]^s\,\mathrm{d}\Sigma\\ &+ \int_{\Omega^{\mathrm{F}}} \rho^0 N^2\frac{(g'\cdot\overline{v}^f)(g'\cdot u^f)}{\|g'\|^2}\,\mathrm{d}x + \int_{\Omega^{\mathrm{F}}} \overline{v}^f\cdot[\nabla p - g'p\rho^0\kappa^{-1}]\,\mathrm{d}x\\ &- \int_{\Omega^{\mathrm{F}}} [\nabla\cdot(\rho^0\overline{v}^f)]S(u)\,\mathrm{d}x - \int_{\Sigma^{\mathrm{FF}}\cup\partial\tilde{X}^{\mathrm{F}}} (\nu\cdot\overline{v}^f)S(u)[\rho^0]^{+}_{-}\,\mathrm{d}\Sigma - \int_{\Sigma^{\mathrm{FS}}} (\nu^{s\to f}\cdot\overline{v}^f)S(u)[\rho^0]^f\,\mathrm{d}\Sigma,\end{aligned} \tag{9}$$

and

$$b_H(u,v) = \int_{\Omega^{\mathrm{S}}} (\overline{v}^s\cdot u^s)\rho^0\,\mathrm{d}x + \int_{\Omega^{\mathrm{F}}} (\overline{v}^f\cdot u^f)\rho^0\,\mathrm{d}x, \tag{10}$$

and

$$c_r(u,v) = \int_{\Omega^{\mathrm{S}}} \overline{v}^s\cdot(\Omega\times u^s)\rho^0\,\mathrm{d}x + \int_{\Omega^{\mathrm{F}}} \overline{v}^f\cdot(\Omega\times u^f)\rho^0\,\mathrm{d}x, \tag{11}$$

where $N^2 = (\nabla\rho^0/\rho^0 - g'\rho^0/\kappa)\cdot g'$ signifies the square of the Brunt-Väisälä frequency; $\nu^{s\to f}$ denotes the normal vector at the fluid-solid boundary pointing from the solid to the fluid side; the symmetrization operation $\mathfrak{S}$ as in de Hoop et al. (2015) is defined as $\mathfrak{S}\{L(u,\overline{v})\} := \frac{1}{2}(L(u,\overline{v}) + L(\overline{v},u))$, for any bilinear form $L(u,v)$. We note that a_2 and b_H in (9) and (10) are analogue of (Shi et al. 2019, (26) and (7)), respectively. We obtain the quadratic eigenvalue problem from (10), (11), (9) and (8):

$$\begin{cases} a_2([u,p,S(u)],v) & = \omega^2 b_H(u,v) - 2\,\mathrm{i}\,\omega c_r(u,v), \\ c_g([u,p],v^p) & = 0. \end{cases} \tag{12}$$

A matrix representation can be derived from (12). In practice, we replace p in a_2 by $p(u^f, u^s_{\Sigma^{\mathrm{FS}}})$ via solving the constraint $c_g([u,p],v^p) = 0$ in (8) and obtain

$$a_2([u, p(u^f, u^s_{\Sigma^{\mathrm{FS}}}), S(u)], v) = \omega^2 b_H(u,v) - 2\,\mathrm{i}\,\omega c_r(u,v). \tag{13}$$

The corresponding orthonormality condition is that, for an eigenpair $(\omega_{(i)}, u^{(i)})$, where (i) denotes the index, any other eigenpair $(\omega_{(j)}, u^{(j)})$ satisfies

$$b_H(u^{(i)}, u^{(j)}) - 2\,\mathrm{i}(\omega_{(i)}^{-1} + \omega_{(j)}^{-1})c_r(u^{(i)}, u^{(j)}) = \delta_{ij}, \tag{14}$$

which is consistent with (Dahlen & Tromp 1998, (4.82)).

Following standard theoretical analysis (de Hoop et al. 2019), we define

$$F(\omega) = -\omega^2 \mathrm{Id} + 2\,\mathrm{i}\,\omega R_\Omega.$$

and consider the quadratic operator pencil

$$L(\omega) = F(\omega) + A_2,$$

where A_2 is defined as $a_2(u,v) = \langle A_2 u, v\rangle$. The decomposition in (6) implies a decomposition of $L(\omega)$,

$$\begin{pmatrix} L_{11}(\omega) & L_{12}(\omega) \\ L_{21}(\omega) & L_{22}(\omega) \end{pmatrix}.$$

In the above, the matrix system corresponds with $L_{11}(\omega)$, while the essential spectrum coincides with the essential spectrum of $L_{22}(\omega)$. Asymptotically, the seismic point spectrum corresponds with the spectrum of $L_{11}(\omega)$.

3 HYDROSTATIC EQUILIBRIUM OF THE LIQUID CORE WITH ROTATION

In this section, we discuss the hydrostatic equilibrium with rotation and how it constrains the shape of boundaries and density distribution in planets. Rotating fluids have been extensively studied (Greenspan 1968; Chandrasekhar 2013; Zhang & Liao 2017). The outer core's properties have been studied through seismic normal modes since the 1970s (Gilbert & Dziewonski 1975; Dziewonski et al. 1975; Dziewonski & Anderson 1981), but also with body waves (Morelli & Dziewonski 1993; Kennett et al. 1995). Much more recently, an alternative radial outer core model has been proposed using the parametrization of the equation of state for liquid iron alloys at high pressures and temperatures, inferred from eigenfrequency observations (Irving et al. 2018). We furthermore mention models for the outer core of the Moon (Weber et al. 2011) and the core of Mars (Rivoldini et al. 2011; Khan et al. 2016) albeit ignoring rotation.

To reach the hydrostatic equilibrium, the prepressure p^0 satisfies

$$\nabla p^0 = \rho^0 g', \tag{15}$$

where g' is defined in (4). Well-posedness requires that

$$\nabla \rho^0 \parallel g' \parallel \nabla p^0 \quad \text{in } \Omega^{\mathrm{F}} \quad \text{and} \quad g' \parallel \nu \quad \text{along } \Sigma^{\mathrm{FS}} \cup \partial \tilde{X}^{\mathrm{F}}; \tag{16}$$

see (de Hoop et al. 2015, Lemma 2.1) for details about the functional properties of ρ^0, p^0 and g'. We provide various approaches forcing (16), in general, in Appendix A yielding the shapes of boundaries of rotating planets.

The computation greatly simplifies upon making an Ansatz for the density distribution, namely, that its level sets are spheroidal. The early study by Clairaut (1743) was based on this Ansatz. We briefly summarize Clairaut's equation for determining the mentioned level sets assuming the ellipticity is small. We let a and $\epsilon(a)$ be the mean radius and ellipticity of the density contours of $\rho^0 = \widehat{\rho}^0(a)$, where $\widehat{\rho}^0(a)$ is the value of the density of a spherically

parameters	Ω (s^{-1})	r_e (km)	$g_{(r_e)}$ (m/s^2)	$\dot{\epsilon}(r_e)$	$\epsilon^{\mathrm{hyd}}_{(r_e)}$	$\epsilon^{\mathrm{obs}}_{(r_e)}$
Earth	$7.2921e{-5}$	6371.0	9.80	$3.05e{-5} > 0$	$3.34e{-3}$	$3.35e{-3}$
Mars	$7.0882e{-5}$	3389.5	3.71	$-8.98e{-5} < 0$	N/A	$5.89e{-3}$

Table 1. Bulk parameters of Earth and Mars; $\dot{\epsilon}(r_e)$ denotes the derivative of ϵ at $a = r_e$, and $\epsilon^{\mathrm{hyd}}_{(r_e)}$ and $\epsilon^{\mathrm{obs}}_{(r_e)}$ denote the computed hydrostatic ellipticity and observed ellipticity, respectively.

symmetric analogue. The ellipticity, ϵ, solves Clairaut's equation,

$$\frac{\mathrm{d}^2\epsilon}{\mathrm{d}a^2} + 8\pi G\widehat{\rho}^0 g_{(a)}^{-1}\left(\frac{\mathrm{d}\epsilon}{\mathrm{d}a} + a^{-1}\epsilon\right) - 6a^{-2}\epsilon = 0, \tag{17}$$

supplemented with the boundary values

$$\left.\frac{\mathrm{d}\epsilon}{\mathrm{d}a}\right|_{a=0} = 0, \quad \left.\frac{\mathrm{d}\epsilon}{\mathrm{d}a}\right|_{a=r_e} = r_e^{-1}\left(\frac{5\Omega^2 r_e}{2g_{(r_e)}} - 2\epsilon_{(r_e)}\right), \tag{18}$$

where $g_{(a)}$ is the value of the reference gravitational field in the radial direction, and r_e is the mean surface radius. The derivation of Clairaut's equation, and the Radau approximation, are put in the context of a general scheme imposing (16) in Appendix A1. The bulk parameters of Earth and Mars are listed in Table 1. While the hydrostatic assumption seems to apply to Earth with reasonable accuracy, $\dot{\epsilon}(r_e)$ of the Mars appears to be negative, whence this assumption fails to hold (Dollfus 1972; Bills & Ferrari 1978).

In Appendix A2, we propose an optimization scheme to constrain the density distribution in the presence of rotation in accordance with (16). With the assumption that the level sets of the density distribution are spheroids, we will recover the solution of Clairaut's equation since (16) will be satisfied. A refined model is the two-layer Maclaurin spheroid (Kong et al. 2010).

4 THE RESULTING QUADRATIC EIGENVALUE PROBLEMS

In this section, we present the matrix representation and solution of the QEP for a rotating planet. In Subsection 4.1, we derive the two matrix forms for a rotating planet with and without fluid regions. The fluid regions often indicate the fluid outer core or the entire core. In Subsection 4.2, we study various numerical approaches to solve the resulting QEP. In Subsection 4.3, we present two different subspace methods to provide solutions for the equivalent linear form of the resulting QEP.

operations	physical relations	corresponding formulae
$(\tilde{v}^s)^{\mathsf{H}} A_{sg} \tilde{u}^s$	solid stiffness matrix with gravity	$\int_{\Omega^{\mathrm{S}}} \nabla \overline{v}_h^s : (c : \nabla u_h^s)\,\mathrm{d}x + \int_{\Sigma^{\mathrm{FS}}} \mathfrak{S}\Big\{ (\overline{v}_h^s \cdot g')(\nu^{s\to f} \cdot u_h^s)[\rho^0]^f \Big\}\,\mathrm{d}\Sigma + \int_{\Omega^{\mathrm{S}}} \mathfrak{S}\Big\{ (\nabla \cdot \overline{v}_h^s)(g' \cdot u_h^s)\rho^0 - u_h^s \cdot (\nabla g') \cdot \overline{v}_h^s \rho^0 - u_h^s \cdot (\nabla \overline{v}_h^s) \cdot g' \rho^0 \Big\}\,\mathrm{d}x$
$(\tilde{v}^f)^{\mathsf{H}} A_f \tilde{u}^s$	Brunt-Väisälä frequency	$\int_{\Omega^{\mathrm{F}}} \rho^0 N^2 \frac{(g' \cdot \overline{v}_h^f)(g' \cdot u_h^f)}{\lVert g' \rVert^2}\,\mathrm{d}x$
$(\tilde{v}^p)^{\mathsf{H}} A_p \tilde{p}$	fluid potential	$\int_{\Omega^{\mathrm{F}}} -\overline{v}_h^p p_h \kappa^{-1}\,\mathrm{d}x$
$(\tilde{v}^f)^{\mathsf{H}} A_{\mathrm{dg}} \tilde{p}$	fluid stiffness matrix with gravity	$\int_{\Omega^{\mathrm{F}}} \Big[\overline{v}_h^f (\nabla p_h) - (\overline{v}_h^f \cdot g') p_h \rho^0 \kappa^{-1} \Big]\,\mathrm{d}x$
$(\tilde{v}^p)^{\mathsf{H}} A_{\mathrm{dg}}^{\mathsf{T}} \tilde{u}^f$	constraint with gravity	$\int_{\Omega^{\mathrm{F}}} \Big[(\nabla \overline{v}_h^p) u_h^f - \overline{v}_h^p (g' \cdot u_h^f) \rho^0 \kappa^{-1} \Big]\,\mathrm{d}x$
$(\tilde{v}^s)^{\mathsf{H}} E_{\mathrm{FS}} \tilde{p}$	fluid-solid boundary condition	$\int_{\Sigma^{\mathrm{FS}}} (\overline{v}_h^s \cdot \nu^{s\to f}) p_h\,\mathrm{d}\Sigma$
$(\tilde{v}^p)^{\mathsf{H}} E_{\mathrm{FS}}^{\mathsf{T}} \tilde{u}^f$	fluid-solid boundary condition	$\int_{\Sigma^{\mathrm{FS}}} -\overline{v}_h^p (\nu^{f\to s} \cdot u_h^s)\,\mathrm{d}\Sigma$
$(\tilde{v}^s)^{\mathsf{H}} M_s \tilde{u}^s$	solid mass matrix	$\int_{\Omega^{\mathrm{S}}} (\overline{v}_h^s \cdot u_h^s) \rho^0\,\mathrm{d}x$
$(\tilde{v}^f)^{\mathsf{H}} M_f \tilde{u}^f$	fluid mass matrix	$\int_{\Omega^{\mathrm{F}}} (\overline{v}_h^f \cdot u_h^f) \rho^0\,\mathrm{d}x$

Table 2. Implicit definition of the matrices for Cowling approximation (cf. (Shi et al. 2019, Table 3)).

4.1 The matrix forms

Following our previous work (Shi et al. 2019), we utilize the mixed finite-element method and FMM (Greengard & Rokhlin 1997; Gimbutas & Greengard 2011; Yokota 2013) to discretize the elastic-gravitational system. It is natural to utilize a mixed finite-element discretization to model the rotation. We use u_h^s, u_h^f and p_h to be the finite-element representation of the dispacement for the solid regions, fluid regions and the pressure, p, respectively. Similarly, v_h^s, v_h^f and v_h^p are the finite-element representations of corresponding test functions. Following the work of Shi et al. (2019), we write $\tilde{u}^s$, $\tilde{u}^f$ and $\tilde{p}$ for the vectors defining u_h^s, u_h^f and p_h, and $\tilde{v}^s$, $\tilde{v}^f$ and $\tilde{v}^p$ for the vectors defining v_h^s, v_h^f and v_h^p. In Tables 2 and 3, we list the submatrices corresponding to the different terms in (12).

operations	physical relations	corresponding formulae
$C_s\tilde{u}^s$	N bodies in $\overline{\Omega^{\mathrm{S}}}$	$\int_{\Omega^{\mathrm{S}}} \nabla\cdot(\rho^0 u_h^s)\,\mathrm{d}x,$ $\int_{\Sigma^{\mathrm{FS}}} (\nu^{f\to s}\cdot u_h^s)\left[\rho^0\right]^s\,\mathrm{d}x,$ $\int_{\Sigma^{\mathrm{SS}}\cup\partial\tilde{X}^{\mathrm{S}}} (\nu\cdot u_h^s)\left[\rho^0\right]_-^+\,\mathrm{d}x$
$C_f\tilde{u}^f$	N bodies in $\overline{\Omega^{\mathrm{F}}}$	$\int_{\Omega^{\mathrm{F}}} \nabla\cdot(\rho^0 u_h^f)\,\mathrm{d}x,$ $\int_{\Sigma^{\mathrm{FS}}} (\nu^{s\to f}\cdot u_h^f)\left[\rho^0\right]^f\,\mathrm{d}x,$ $\int_{\Sigma^{\mathrm{FF}}\cup\partial\tilde{X}^{\mathrm{F}}} (\nu\cdot u_h^f)\left[\rho^0\right]_-^+\,\mathrm{d}x$
$S(C\tilde{u})$	solution for Poisson's equation	$G\int_{\tilde{X}} \frac{\nabla'\cdot(\rho^0(x')u_h(x'))}{\|x-x'\|}\,\mathrm{d}x'$ $+G\int_{\Sigma\cup\partial\tilde{X}} \frac{\nu(x')\cdot u_h(x')[\rho^0(x')]_-^+}{\|x-x'\|}\,\mathrm{d}x'$
$(\tilde{v}^s)^{\mathsf{H}}C_s^{\mathsf{T}}(SC\tilde{u})$	incremental gravitational field in $\overline{\Omega^{\mathrm{S}}}$	$\int_{\Omega^{\mathrm{S}}} \nabla\cdot(\rho^0\overline{v}_h^s)S(u_h)\,\mathrm{d}x$ $+\int_{\Sigma^{\mathrm{FS}}} (\overline{v}_h^s\cdot\nu^{f\to s})S(u_h)[\rho^0]^s\,\mathrm{d}x$ $+\int_{\Sigma^{\mathrm{SS}}\cup\partial\tilde{X}^{\mathrm{S}}} (\overline{v}_h^s\cdot\nu)S(u_h)[\rho^0]_-^+\,\mathrm{d}x$
$(\tilde{v}^s)^{\mathsf{H}}C_f^{\mathsf{T}}(SC\tilde{u})$	incremental gravitational field in $\overline{\Omega^{\mathrm{F}}}$	$\int_{\Omega^{\mathrm{F}}} \nabla\cdot(\rho^0\overline{v}_h^f)S(u_h)\,\mathrm{d}x$ $+\int_{\Sigma^{\mathrm{FS}}} (\overline{v}_h^f\cdot\nu^{s\to f})S(u_h)[\rho^0]^f\,\mathrm{d}x$ $+\int_{\Sigma^{\mathrm{FF}}\cup\partial\tilde{X}^{\mathrm{F}}} (\overline{v}_h^f\cdot\nu)S(u_h)[\rho^0]_-^+\,\mathrm{d}x$
$(\tilde{v}^s)^{\mathsf{H}}R_s\tilde{u}^s$	rotation in Ω^{S}	$\int_{\Omega^{\mathrm{S}}} \overline{v}_h^s\cdot\big(\Omega\times u_h^s\big)\rho^0\,\mathrm{d}x$
$(\tilde{v}^f)^{\mathsf{H}}R_f\tilde{u}^f$	rotation in Ω^{F}	$\int_{\Omega^{\mathrm{F}}} \overline{v}_h^f\cdot\big(\Omega\times u_h^f\big)\rho^0\,\mathrm{d}x$

Table 3. Implicit definition of the matrices for self gravitation and rotation (cf. (Shi et al. 2019, Table 4)).

4.1.1 Planets with fluid regions

Following our previous work (Shi et al. 2019), for the planets with fluid regions, we have the matrix representation

$$\omega^2 M\tilde{u} - 2\,\mathrm{i}\,\omega\tilde{R}_\Omega\tilde{u} - (A_G - E_G A_p^{-1}E_G^{\mathsf{T}} - C^{\mathsf{T}}SC)\tilde{u} = 0, \tag{19}$$

with

$$A_G = \begin{pmatrix} A_{sg} & 0 \\ 0 & A_f \end{pmatrix},\ \tilde{R}_\Omega = \begin{pmatrix} R_s & 0 \\ 0 & R_f \end{pmatrix},\ E_G = \begin{pmatrix} E_{\mathrm{FS}} \\ A_{\mathrm{dg}} \end{pmatrix},$$

$$M = \begin{pmatrix} M_s & 0 \\ 0 & M_f \end{pmatrix},\ C = \begin{pmatrix} C_s & C_f \end{pmatrix},\ \tilde{u} = \begin{pmatrix} \tilde{u}^s \\ \tilde{u}^f \end{pmatrix},$$

where all the submatrices are shown in Tables 2 and 3. We note that (19) is the matrix representation of (12).

4.1.2 Planets without fluid regions

For a purely solid planet, (19) simplifies and we obtain the QEP,

$$\omega^2 M_s \tilde{u}^s - 2\,\mathrm{i}\,\omega R_s \tilde{u}^s - (A_{sg} - C_s^{\mathsf{T}} S_s C_s)\tilde{u}^s = 0. \tag{20}$$

We note that A_{sg}, C_s and C_s^{T} are shown in Tables 2 and 3 and do not include any terms related to the fluid-solid boundaries.

4.2 Solution of the quadratic eigenvalue problem

To simply (19) and (20) without any loss of the generality, we let $\tilde{u}$ be the solution vector $\tilde{u}^s$ for (20) or $\tilde{u}$ for (19) and derive a standard form for the QEP,

$$\omega^2 M\tilde{u} - 2\,\mathrm{i}\,\omega \tilde{R}_\Omega \tilde{u} - A\tilde{u} = 0, \tag{21}$$

where A represents either $A_{sg} - C_s^{\mathsf{T}} S_s C_s$ in (20) or $A_G - E_G A_p^{-1} E_G^{\mathsf{T}} - C^{\mathsf{T}} S C$ in (19). We also note that $\tilde{R}_\Omega = -\tilde{R}_\Omega^{\mathsf{T}}$.

It is challenging to solve the resulting QEP directly; see Tisseur & Meerbergen (2001) for a review and Bai et al. (2000) for a practical guide. The standard QEP takes the form of

$$(\omega^2 M + \omega \mathtt{C} + K)\tilde{u} = 0,$$

where $\mathtt{C} = -2\,\mathrm{i}\,\tilde{R}_\Omega$ with $\mathtt{C} = \mathtt{C}^{\mathsf{H}}$ and $K = -A$ with $K = K^{\mathsf{H}}$ while comparing with our problem (21). The eigenfrequencies are real and come in pairs $(\omega, -\omega)$. To solve the QEP of the original form, the QEP is often projected onto a properly chosen low-dimensional subspace to facilitate the reduction to a QEP directly with lower dimension, such as the Jacobi–Davidson method (Sleijpen et al. 1996a,b). The reduced QEP can then be solved by a standard dense matrix technique. Both Arnoldi- and Lanczos-type processes (Hoffnung et al. 2006) were developed to build projections of the QEP. A subspace approximation method (Holz et al. 2004) was presented using perturbation theory of the QEP. A second-order Arnoldi procedure for generating an orthonormal basis has been developed for solving a large-scale QEP directly (Bai & Su 2005). However, the above-mentioned methods typically utilize a shift-and-invert scheme to solve for the interior eigenpairs. In practice, solving shifted linear systems often leads to a computational bottleneck, especially, on a highly parallel supercomputer with distributed memory using a direct solver. We examplify this issue in Shi et al. (2018).

Alternatively, the QEP can be transformed into an equivalent linear problem. Possible options are the following (Saad 2011, Chapter 9.3)

$$\begin{pmatrix} 0 & I \\ -A & -2\tilde{R}_\Omega \end{pmatrix} \begin{pmatrix} \tilde{u} \\ \mathrm{i}\,\omega\tilde{u} \end{pmatrix} = \mathrm{i}\,\omega \begin{pmatrix} I & 0 \\ 0 & M \end{pmatrix} \begin{pmatrix} \tilde{u} \\ \mathrm{i}\,\omega\tilde{u} \end{pmatrix}, \tag{22}$$

$$\begin{pmatrix} 0 & A \\ A & 2\tilde{R}_\Omega \end{pmatrix} \begin{pmatrix} \tilde{u} \\ \mathrm{i}\,\omega\tilde{u} \end{pmatrix} = \mathrm{i}\,\omega \begin{pmatrix} A & 0 \\ 0 & -M \end{pmatrix} \begin{pmatrix} \tilde{u} \\ \mathrm{i}\,\omega\tilde{u} \end{pmatrix}, \tag{23}$$

$$\begin{pmatrix} 0 & I \\ A & 2\,\mathrm{i}\,\tilde{R}_\Omega \end{pmatrix} \begin{pmatrix} \tilde{u} \\ \omega\tilde{u} \end{pmatrix} = \omega \begin{pmatrix} I & 0 \\ 0 & M \end{pmatrix} \begin{pmatrix} \tilde{u} \\ \omega\tilde{u} \end{pmatrix}, \tag{24}$$

$$\begin{pmatrix} A & 0 \\ 0 & M \end{pmatrix} \begin{pmatrix} \tilde{u} \\ \omega\tilde{u} \end{pmatrix} = \omega \begin{pmatrix} -2\,\mathrm{i}\,\tilde{R}_\Omega & M \\ M & 0 \end{pmatrix} \begin{pmatrix} \tilde{u} \\ \omega\tilde{u} \end{pmatrix}, \tag{25}$$

$$\begin{pmatrix} 0 & A \\ A & 2\,\mathrm{i}\,\tilde{R}_\Omega \end{pmatrix} \begin{pmatrix} \tilde{u} \\ \omega\tilde{u} \end{pmatrix} = \omega \begin{pmatrix} A & 0 \\ 0 & M \end{pmatrix} \begin{pmatrix} \tilde{u} \\ \omega\tilde{u} \end{pmatrix}. \tag{26}$$

The orthonormality condition (cf. (14)) implies

$$\tilde{u}_{(i)}^{\mathsf{H}} M \tilde{u}_{(j)} - 2\,\mathrm{i}\,(\omega_{(i)} + \omega_{(j)})^{-1} \tilde{u}_{(i)}^{\mathsf{H}} \tilde{R}_\Omega \tilde{u}_{(j)} = \delta_{ij}, \tag{27}$$

where $(i), (j)$ are indices of the two eigenvectors. In Table 4, we list the features of the different forms while solving the QEP. We will work with (26).

systems	Hermitian or not	concerns
(22)	a real non-Hermitian system	non-Hermitian & orthonormality
(23)	a real non-Hermitian system	the non-positive “new” mass matrix
(24)	a complex non-Hermitian system	non-Hermitian & orthonormality
(25)	a complex Hermitian system	the non-positive “new” mass matrix
(26)	a complex Hermitian system	the non-positive “new” mass matrix

Table 4. List of features of different linear forms.

4.3 Subspace approximation

Following (Shi et al. 2018, 2019) using x as an alternative notation for the displacement vector of a non-rotating planet, we first solve for the eigenpairs in

$$Ax = \omega_{[2]}^2 Mx, \tag{28}$$

where $\omega_{[2]}$ denotes the eigenfrequency for the linear real Hermitian problem. Polynomial filtering techniques (Saad 2006; Fang & Saad 2012; Li et al. 2016) are appealing as they do not involve solving linear systems with highly indefinite shifted matrices. Instead, the bulk of the computations are carried out in the form of matrix-vector multiplications, which are generally much easier to be parallelized than solving the indefinite linear systems. For a generalized eigenvalue problem, $Ax = \lambda Mx$ with both real Hermitian A and M, the base form of filtering is

$$\rho(M^{-1}A)x = \rho(\lambda)x,$$

where $\rho(\cdot)$ denotes the filter function (Li et al. 2016; Shi et al. 2018). Multiplying both sides by M yields the following problem

$$K_2 x = \rho(\lambda)Mx, \quad \text{with} \quad K_2 = M\rho(M^{-1}A).$$

We apply the Lanczos algorithm to matrix pencil (K_2, M). In the polynomial filtered non-restart Lanczos algorithm, each step of the iterative process consists of a Lanczos step with K_2,

$$\beta_{i+1}z_{i+1} = K_2 v_i - \alpha_i z_i - \beta_i z_{i-1},$$

followed by a full reorthogonalization against all the previous vectors $\{v\}$ using modified Gram-Schmidt iterations with z is defined as $z = Mv$. A test for convergence is implemented for every N_{cycle} steps after the first N_{test} iterations. We check if the sum of the Ritz values that are greater than the threshold τ no longer vary in several consecutive checks. Finally, a computed Ritz pair (λ_i, x_i) is accepted if λ_i is in the desired interval and its residual norm is smaller than a given tolerance. We note that vectors v and z are real and their inner product is $(v, z) = v^\mathsf{T} z$. Since K_2 and M are real Hermitian, α and β, in the tridiagonal matrix T_{K_2} say, are real. The details of the algorithm are provided in Algorithm 1 from line 1 to 12.

In the above, $\{v\}$ contains the extended Lanczos vectors. These generate a large subspace, spanned by eigenvectors, associated with a target interval. In Subsections 4.3.1 and 4.3.2, we utilize the computed extended Lanczos vectors to reduce the dimension of the equivalent form (26) of the QEP.

4.3.1 Extended Lanczos vectors spanning the subspace

Instead of using the computed Ritz vectors directly, we utilize extended Lanczos vectors and obtain more Ritz vectors through the polynomial filtering method. We then approximate the solution $\tilde{u}$ using the basis computed from

$$AX_e = MX_e\Lambda_e, \tag{29}$$

where X_e denotes the Ritz vectors of the linear system and Λ_e denotes a diagonal matrix whose diagonal is a collection of $\omega_{[2]}^2$. We take m_e eigenvectors spanning a subspace and let $\tilde{u}_e = X_e y_e$ to approximate $\tilde{u}$ in (21), where y_e is complex. Applying

$$\begin{pmatrix} X_e^\mathsf{T} & 0 \\ 0 & X_e^\mathsf{T} \end{pmatrix}$$

to both sides of (26) and making use of $X_e^\mathsf{T} A X_e = \Lambda_e$, we can then rewrite (26) as

$$\begin{pmatrix} 0 & \Lambda_e \\ \Lambda_e & 2\,\mathrm{i}\,X_e^\mathsf{T}\tilde{R}_\Omega X_e \end{pmatrix} \begin{pmatrix} y_e \\ \omega_e y_e \end{pmatrix} = \omega_e \begin{pmatrix} \Lambda_e & 0 \\ 0 & I \end{pmatrix} \begin{pmatrix} y_e \\ \omega_e y_e \end{pmatrix}. \tag{30}$$

We note that $2\,\mathrm{i}\,X_e^\mathsf{T}\tilde{R}_\Omega X_e$ is dense with size of $m_e \times m_e$ and complex Hermitian. We can further simplify (30) to a standard eigenvalue problem,

$$\begin{pmatrix} 0 & \Lambda_e^{1/2} \\ \Lambda_e^{1/2} & 2\,\mathrm{i}\,X_e^\mathsf{T}\tilde{R}_\Omega X_e \end{pmatrix} \begin{pmatrix} \Lambda_e^{1/2} y_e \\ \omega_e y_e \end{pmatrix} = \omega_e \begin{pmatrix} \Lambda_e^{1/2} y_e \\ \omega_e y_e \end{pmatrix}. \tag{31}$$

It is apparent that if $\tilde{R}_\Omega = 0$, we have $\omega_e = \omega_{[2]} = \Lambda_e^{1/2}$. The system (31) can be solved via the standard eigensolver that was implemented in `LAPACK` (Anderson et al. 1999). The details are provided in lines 13 to 20 in Algorithm 1.

Algorithm 1 A subspace method for the resulting QEP

```
 1: Input: $A$ and $M$, filter function $\rho$, $K_2 = \rho(A)$ and target interval $[f_1, f_2]$
 2: Initialization: $z_0 := 0$, initial vector $v_1$ with $\|v_1\|_M = 1$, and $z_1 := Mv_1$
 3: for $i = 1, \ldots, N_{\mathrm{MaxIts}}$ do
 4:     $z := K_2 v_i - \beta_i z_{i-1}$, $\alpha_i = (z, v_i)$, $z := z - \alpha_i z_i$
 5:     $z := z - \sum_j (z, v_j) z_j$ for $j \le i$                    (full reortho.)
 6:     $v := M^{-1} z$, $\beta_{i+1} = (v, z)^{1/2}$, $v_{i+1} := v/\beta_{i+1}$, $z_{i+1} := z/\beta_{i+1}$
 7:     if $i \le N_{\mathrm{test}}$ and $\mod (i - N_{\mathrm{test}}, N_{\mathrm{cycle}}) = 0$ then
 8:         $t_{\mathrm{old}} = t_{\mathrm{new}}$ and $t_{\mathrm{new}} = \sum \theta_j$ for $\theta_j \ge \tau$, where $\theta_j$ is the Ritz value
 9:         if $(|t_{\mathrm{new}} - t_{\mathrm{old}}| < \mathrm{tol}_0)$ break; end if
10:     end if
11: end for
12: Obtain all the Lanczos vectors $V = [v_1, \ldots, v_{m_l}]$
13: $[\Theta_A, Q_A] = \mathrm{eig}(T_A)$, where $T_A = VAV^{\mathsf{T}}$
14: for $i = 1, \ldots, m_l$ do
15:     $x_i = VQ_A(:, i)$, $x_i := x_i/\|x_i\|_M$ and $\lambda_i := (Ax_i, x_i)$
16:     if $(\lambda_i \ge \xi_{cut}$ and $\|Ax_i - \lambda_i M x_i\|/|\lambda_i| < \mathrm{tol}_2)$ Accept $(\lambda_i, x_i)$; end if
17: end for
18: Obtain $X_e = [x_1, \ldots, x_{m_e}]$ and $\Lambda_e = [\lambda_1, \ldots, \lambda_{m_e}]$
19: $[\omega_e, Y_e] = \mathrm{eig}(A_e)$, where $A_e = \begin{pmatrix} 0 & \Lambda_e^{1/2} \\ \Lambda_e^{1/2} & 2\,\mathrm{i}\, X_e^{\mathsf{T}} \tilde{R}_\Omega X_e \end{pmatrix}$
20: Collect all the eigenfrequencies in $[f_1, f_2]$ as well as the corresponding eigenvectors
```

4.3.2 Extended Lanczos vectors in the Cowling approximation spanning the subspace

The computation of the incremental gravitational potential using the FMM is quite costly. To avoid this computation one may invoke the Cowling approximation. Then we solve the generalized eigenvalue problem

$$A_C x = \omega_C^2 M x,$$

where

$$A_C = A + C^{\mathsf{T}} S C,$$

for a planet containing fluid regions (cf. (19)) and

$$A_C = A + C_s^{\mathsf{T}} S_s C_s,$$

for an entirely solid planet (cf. (20)), while ω_C denotes the eigenfrequencies in the Cowling approximation. We collect all the computed Lanczos vectors and obtain $V_C = [v_1, \dots, v_{m_{l_c}}]$, where m_{l_c} is the number of computed Lanczos vectors. We calculate the extended Ritz vectors $X_c = [x_1, \dots, x_{m_c}]$, where m_c is the number of Ritz vectors, for the original system without rotation via

$$AX_c = MX_c\Lambda_c,$$

where Λ_c denotes a diagonal matrix. The solution $\tilde{u}$ of (21) can now be approximated by $\tilde{u}_c = X_c y_c$, where y_c is complex. The counterpart of (31) is obtained upon projecting (21) onto the proposed subspace X_c,

$$\begin{pmatrix} 0 & \Lambda_c^{1/2} \\ \Lambda_c^{1/2} & 2\,\mathrm{i}\,X_c^{\mathsf{T}}\tilde{R}_\Omega X_c \end{pmatrix} \begin{pmatrix} \Lambda_c^{1/2} y_c \\ \omega_c y_c \end{pmatrix} = \omega_c \begin{pmatrix} \Lambda_c^{1/2} y_c \\ \omega_c y_c \end{pmatrix}. \tag{32}$$

In Algorithm 2, we provide the details of our proposed algorithm.

Algorithm 2 A subspace method using Lanczos vectors of Cowling approximation

```
Input: $A_C$, $A$ and $M$, filter function $\rho$, $K_C = \rho(A_C)$ and target interval $[f_1, f_2]$
Initialization: $z_0 := 0$, initial vector $v_1$ with $\|v_1\|_M = 1$, and $z_1 := Mv_1$
Perform filtered Lanczos algorithm $\beta_{i+1}z_{i+1} = K_C v_i - \alpha_i z_i - \beta_i z_{i-1}$ (cf. Algorithm 1)
Obtain all the Lanczos vectors $V_C = [v_1, \dots, v_{m_{l_c}}]$
$[\Theta_C, Q_C] = \mathrm{eig}(T_C)$, where $T_C = V_C^{\mathsf{T}} A_C V_C$
for $i = 1, \dots, m_{l_c}$ do
    $x_i = VQ_C(:, i)$, $x_i := x_i/\|x_i\|_M$ and $\lambda_i := (Ax_i, x_i)$
    if ($\lambda_i \geq \xi_{cut}$ and $\|Ax_i - \lambda_i Mx_i\|/|\lambda_i| < \mathrm{tol}_3$) Accept $(\lambda_i, x_i)$; end if
end for
Obtain $X_c = [x_1, \dots, x_{m_c}]$ and $\Lambda_c = [\lambda_1, \dots, \lambda_{m_c}]$
$[\omega_c, Y_c] = \mathrm{eig}(A_c)$, where $A_c = \begin{pmatrix} 0 & \Lambda_c^{1/2} \\ \Lambda_c^{1/2} & 2\,\mathrm{i}\,X_c^{\mathsf{T}}\tilde{R}_\Omega X_c \end{pmatrix}$
Collect all the eigenfrequencies in $[f_1, f_2]$ as well as the corresponding eigenvectors
```

4.3.3 Summary and comparison with other approaches

In our proposed method, the key is to find a good subspace to project the full QEP onto preserving accuracy. The subspaces X_e, X_c are contained in H_1 up to discretization errors.

Several competing approaches were studied during the past several decades. The perturbation theory (Dahlen & Sailor 1979) utilizes the eigenfunctions of a spherically symmetric Earth model to estimate first- and second-order Coriolis splitting, splitting due to rotation

model	# of elm.	size of A_p	size of A	size of S	$[f_1, f_2]$ (mHz)
Constant (C3kp1)	3,129	0	1,821	3,521	[0.35,0.85]
Earth (E3kp1)	3,330	392	2,760	4,242	[0.3,0.86]
Mars (M2kp1)	1,887	145	1,677	2,539	[0.4,1.14]
Mars (M8kp1)	8,020	152	7,557	12,436	[0.4, 1.14]
Earth (E40kp1)	42,828	3,171	30,384	51,000	[0.1,1.5]

Table 5. Numerical parameter values pertaining to the testing of computational accuracy and estimating the cost in different models.

and ellipticity (Dahlen & Tromp 1998, Chapter 14.2 and Appendix D.4). There are two limitations in the perturbation theory: First, the basis from a spherically symmetric model does not lie in H_1, in general, if the shapes of the fluid-solid boundaries are not spherical; secondly, the calculation relies on the fact that the rotation frequency must be much smaller than the eigenfrequencies. The self-coupling and group-coupling approaches, and the later implemented full-mode coupling method (Deuss & Woodhouse 2001, 2004; Al-Attar et al. 2012; Yang & Tromp 2015; Akbarashrafi et al. 2017) have the drawback that their underlying basis fundamentally does not lie in H_1 which is particularly important in the presence of fluid-solid boundaries. As an aside, our approach allows high rotation rates. Nonetheless, our approach based on extended Lanczos vectors is not entirely dissimilar from a full-mode coupling concept.

5 COMPUTATIONAL EXPERIMENTS

In this section, we first show the computational accuracy of tour proposed approach on different small planetary models when the computation of the full mode expansion is feasible. We then illustrate computational experiments yielding planetary normal modes with the use of two supercomputers, Stampede2 (an Intel cluster) at the Texas Advanced Computing Center and Abel (a Cray XC30 cluster) at Petroleum Geo-Services. We study the spectra of two models: Earth 1066A (Gilbert & Dziewonski 1975) and a Mars model (Khan et al. 2016). We use 23.9345 hours (Allen 1973) and 24.6229 hours (Lodders & Fegley 1998) as Earth's and Mars' rotation periods, respectively.

5.1 Computational accuracy

For small models, we are able to compute the full mode expansion associated with the point spectrum using (31). In Table 5, we list the numerical parameter values pertaining to the testing of computational accuracy and estimating the cost in different models: The number

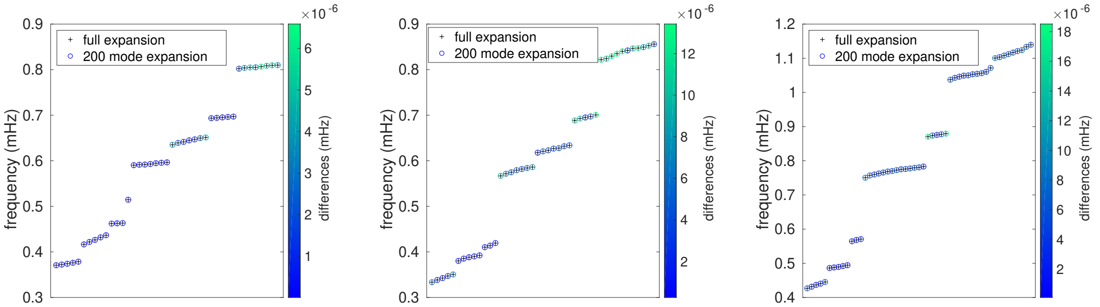

(a) constant (C3kp1) (b) Earth (E3kp1) (c) Mars (M2kp1)

Figure 4. Tests with three different small models for the low-lying seismic eigenfrequencies. The numerical parameters of the tests are given in Table 5.

of elements (labeled as # of elm.), size of A_p, size of A, size of S and the target frequency interval in milliHertz (labeled as $[f_1, f_2]$ (mHz)).

In Figs. 4 (a)–(c), we illustrate the computational accuracy of tests in three different models C3kp1, E3kp1 and M2kp1, respectively, on the lowest seismic eigenfrequencies using P1 elements. We compare the differences in the eigenfrequencies between the full mode expansion and a 200 mode expansion using Algorithm 1. The differences are about 5×10^{-6} mHz, which is two digits below the accuracy of common normal mode measurements.

In Figs. 5 (a) and (b), we show the computational accuracy of M8kp1 on [0.4, 1.14] mHz as well as the error distribution. In Fig. 5 (a), we show that even with a 100 mode expansion, the differences are as low as 1×10^{-5} mHz. In Fig. 5 (b), we show that with a 1000 mode expansion, the differences are further reduced to about 1×10^{-6} mHz.

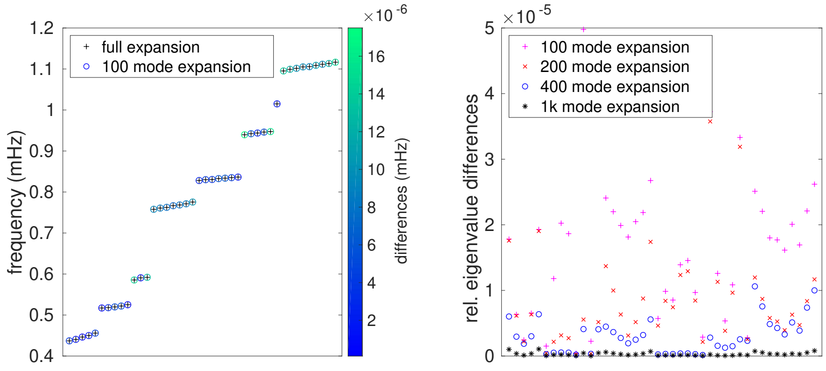

(a) M8kp1 on [0.4, 1.14]mHz (b) Errors of (a)

Figure 5. Tests for computational accuracy of a Mars model using different numbers of mode expansion.

Methods	pol. deg.	# of iter.	t-Mv (s)	t-FMM (s)	total times (s)	rel. errs
Algorithm 1	167	831	$1.8e{-}4$	$5.4e{-}1$	79274.0	$5.e{-}7$
Algorithm 2	108	771	$1.7e{-}4$	$5.5e{-}1$	1761.0	$2.e{-}6$

Table 6. Comparison between two methods on experiment E40kp1 in Table 5 on 4 computing nodes.

5.2 Computational cost

Here, we compare the computational costs of Algorithms 1 and 2. In Table 6, we list the parameters used in running the two algoritms on experiment E40kp1: Polynomial degree (labeled as pol. deg.), number of iterations (labeled as # of iter.), average time of one M multiplication with a vector (labeled as t-Mv), average time of one FMM operation (labeled as t-FMM), total time and relative error that are calculated via $\|\omega^2 M\tilde{u} - 2\,\mathrm{i}\,\omega\tilde{R}_\Omega\tilde{u} - A\tilde{u}\|/\|\omega\|$. Both tests are performed on 4 Intel Knights Landing nodes using P1 elements. We note that the computational cost of one FMM operation is much longer than this of the sparse matrix-vector multiplication. In this test, Algorithms 1 and 2 perform 167×831 = 138,777 FMM operations and 771 FMM operations, respectively. The cost savings in the Cowling approximation are significant indeed.

5.3 Benchmark experiments for Earth models

Here, we perform a benchmark experiment of Earth model 1066A (Gilbert & Dziewonski 1975) against a perturbation calculation (Dahlen & Sailor 1979). In the perturbation calculation, the eigenfrequency perturbations $\delta\omega_m$ have a following form

$$\delta\omega_m = \omega_0(a + bm + cm^2), \quad -l \le m \le l, \tag{33}$$

where ω_0 denotes the eigenfrequency of the unperturbed spherically symmetric model, l denotes the angular order in the spherical harmonic expansion, and a, b and c are the relevant coefficients. The values of a, b and c for different radial modes can be found in (Dahlen & Tromp 1998, Table 14.1). In Table 7, we list the numerical parameters of the Earth models in the benchmark test. Models E1Mp1 and E2Mp2 used to compute ω_0 represent spherically symmetric Earth models without rotation. Experiments EE1Mp1 and EE2Mp2 represent elliptic Earth models and are used to compute eigenfrequencies of our proposed method via Algorithm 2. The ellipticity of the Earth models are computed by solving Clairaut's equation in Section 3. Since the eigenfrequencies of the Slichter modes

Exp.	# of elm.	size of A_p	size of A	size of S	$[f_1, f_2]$ (mHz)
Earth (E1Mp1)	1,011,973	31,849	537,198	1,074,577	[0.04,1.5]
Earth (E2Mp2)	2,015,072	530,721	8,569,197	2,165,360	[0.2,1.5]
Earth (EE1Mp1)	1,003,065	31,688	533,064	1,065,629	[0.04,1.5]
Earth (EE2Mp2)	2,002,581	528,124	8,520,432	2,153,109	[0.2,1.5]

Table 7. Numerical parameters of the Earth models used in the benchmark experiments.

(Slichter 1961) are close to the upper bound of the essential spectrum and the convergence of the proposed algorithm is relatively slow, we set $f_1 = 0.04$ mHz and use experiments E1Mp1 and EE1Mp1 to compute the Slichter modes using P1 elements. Experiments E2Mp2 and EE2Mp2 are used to compute other modes using P2 elements. It is expected that rotation through Coriolis coupling of low-frequency modes is the dominant mechanism (Zürn et al. 2000). In Fig. 6, we show the comparison between the perturbation and our proposed method. The values of the computed eigenfrequenies of the proposed method agree with the perturbation results in as much as that the relative differences are commonly less than 0.3 μHz. The degree of agreement is, of course, model dependent.

5.4 Mars models

Here, we present our computational results for Mars models. The interiors of the Mars models are based on mineral physics calculations (Khan et al. 2016). In Table 8, we list three Mars models labeled as M2Mp2, EM2Mp2 and TM2Mp2 which represent a spherically symmetric Mars model without rotation, a spheroidal Mars model with rotation, and a spheroidal Mars model with a three-dimensional crust and rotation using P2 elements. The shape of the spheroidal Mars model's core-mantle boundary is computed by solving Clairaut's equation. Since Mars presumably is not hydrostatic as discussed in Section 3, its solid region is estimated via a linear interpolation using the ellipticities of the core-mantle boundary ($\varepsilon = 4.19 \times 10^{-3}$) and the surface ($\varepsilon = 5.89 \times 10^{-3}$). Model TM2Mp2 is illustrated in Fig. 2.

In Fig. 7, we show eigenfrequencies computed in different Mars models listed in Table 8. Symbols $\bullet$, $\circ$ and $\times$ represent the eigenfrequencies computed in Mars models M2Mp2,

Exp.	# of elm.	size of A_p	size of A	size of S	$[f_1, f_2]$ (mHz)
Mars (M2Mp2)	1,996,773	579,338	8,967,684	2,257,801	[0.2,2.0]
Mars (EM2Mp2)	2,001,619	579,667	8,984,532	2,262,143	[0.2,2.0]
Mars (TM2Mp2)	2,008,654	323,810	8,289,927	2,158,366	[0.2,2.0]

Table 8. Numerical parameters for the Mars models.

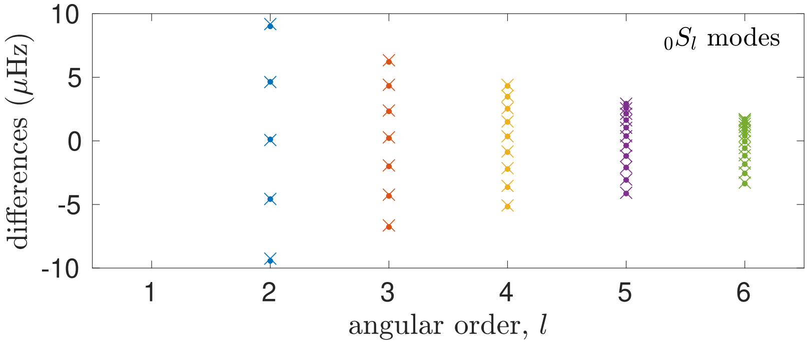

(a) Comparison of ${}_0S_l$ modes

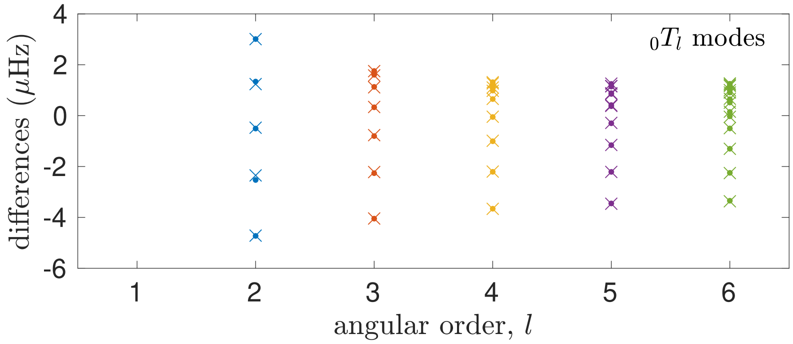

(b) Comparison of ${}_0T_l$ modes

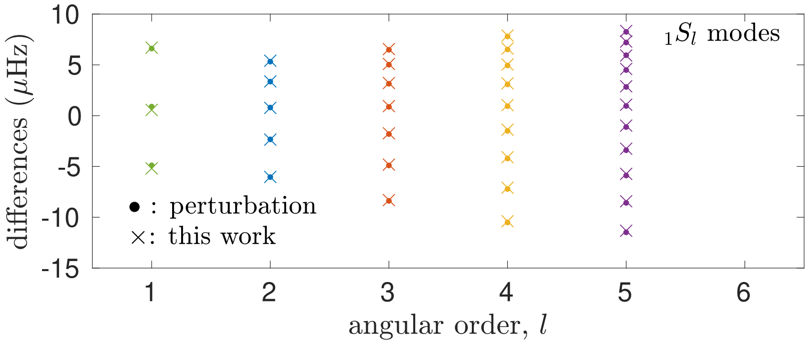

(c) Comparison of ${}_1S_l$ modes

Figure 6. Comparison of the results from perturbation calculation and our proposed method, which are shown using symbols • and ×, respectively. (a), (b) and (c) present comparisons of ${}_0S_l$, ${}_0T_l$ and ${}_1S_l$ modes, respectively.

EM2Mp2 and TM2Mp2 (cf. Table 8). The horizontal dashed lines represent the eigenfrequencies of a spherically symmetric Mars model computed with a one-dimensional solver (Masters et al. 2011; Ye 2018). Mode splitting is apparent due to ellipticity, rotation and heterogeneity in three dimensions. The three-dimensional crust does not have a clear influence on the lowest eigenfrequencies associated with ${}_0S_2$, ${}_0T_2$, ${}_1S_1$, ${}_0S_3$, ${}_0T_3$, ${}_1S_2$ and ${}_0S_4$ in Fig. 7 (a). The three-dimensional crust has a noticeable effect on the surface wave modes, such as ${}_0T_6$, ${}_0T_7$, ${}_0T_8$, ${}_0S_6$, ${}_0S_7$ and ${}_0S_8$, as expected. In Fig. 8, we show the eigenfrequencies

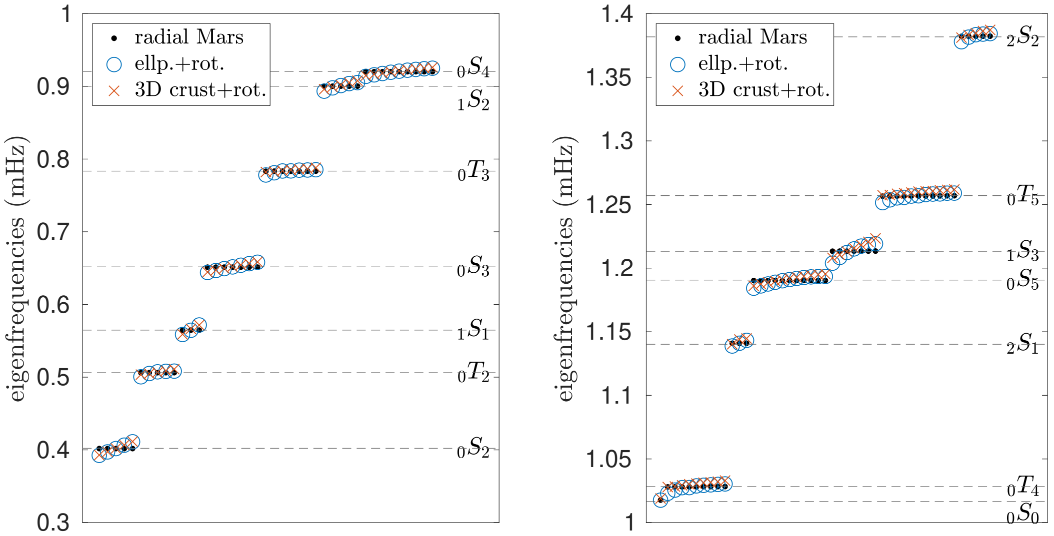

(a) modes in [0.3, 1.0]mHz

(b) modes in [1.0, 1.4]mHz

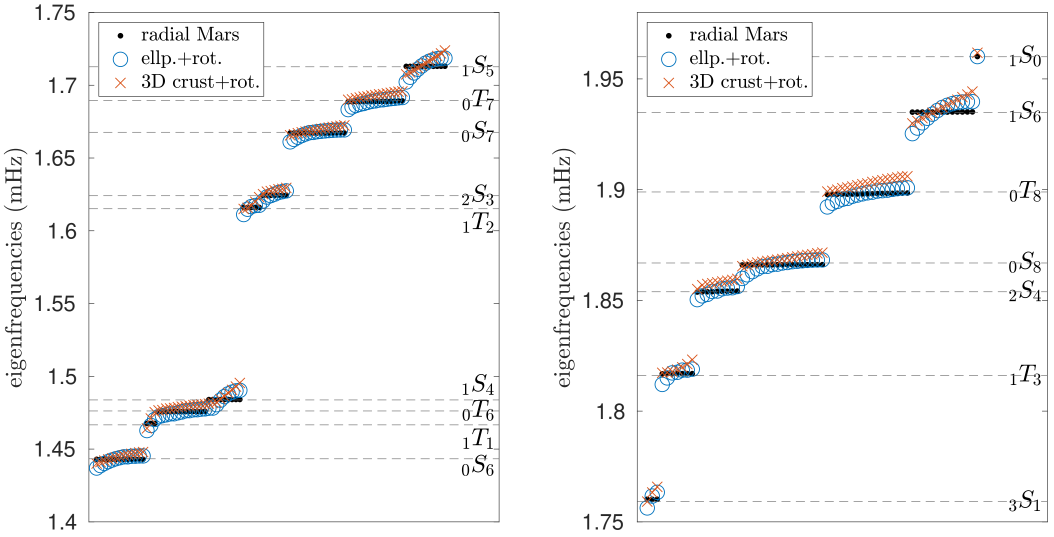

(c) modes in [1.4, 1.75]mHz

(d) modes in [1.75, 1.95]mHz

Figure 7. Eigenfrequencies of different Mars models. (a), (b), (c) and (d) illustrate eigenfrequencies in different frequency windows. Symbols •, ∘ and × represent the eigenfrequencies computed from Mars models M2Mp2, EM2Mp2 and TM2Mp2 in Table 8, respectively. The horizontal dashed lines represent the eigenfrequencies of a spherically symmetric Mars model computed with a one-dimensional solver.

in a subinterval of the interval used in Fig. 7 (d). Here, we note the splitting of modes $_2S_4$, $_0S_8$ and $_0T_8$ and highlight the effects of the three-dimensional crust. The maximum difference among the eigenfrequencies in Fig. 8 is 5.2 μHz, which, in principle, can be detected. There is no mode-coupling observed in these experiments. In Fig. 9, we plot the branch $_1S_l$ as well as the corresponding incremental gravitational fields $\nabla S(u)$. We anticipate that

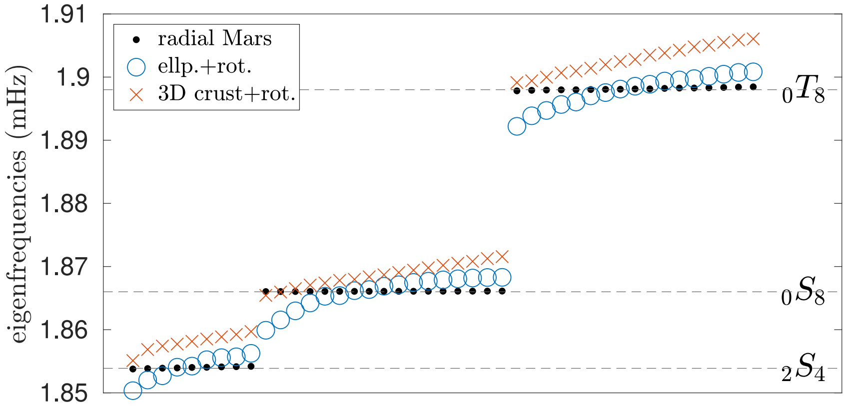

Figure 8. Illustration of a subinterval in Fig. 7(d). Splitting of modes $_2S_4$, $_0S_8$ and $_0T_8$ due to the three-dimensional crust. The maximum difference among the eigenfrequencies is 5.2 μHz.

both the seismic and gravity measurements of these modes could help to estimate the size of Martian core.

6 CONCLUSION

In this work, we propose a method to compute the normal modes of a fully heterogeneous rotating planet. We apply the mixed finite-element method to the elastic-gravitational system of a rotating planet and utilize the FMM to calculate the self gravitation. We successfully separate out the essential spectrum by introducing an additional constraint equation. Thus, we are able to compute the normal modes associated with seismic point spectrum. To solve the relevant QEP, we utilize extended Lanczos vectors computed in a non-rotating planet – with the shape of boundaries of a rotating planet and accounting for the centrifugal potential – spanning a subspace to reduce the dimension of an equivalent linear form of the QEP. The reduced system can be solved with a standard eigensolver. We demonstrate our ability to compute the seismic normal modes with rotation accurately. We then study the computational accuracy and cost of our proposed method and use a standard Earth model to perform a benchmark test against a perturbation calculation. We carry out computational experiments on various Mars models and illustrate mode splitting due to rotation, ellipticity and heterogeneity of the crust. The use of modern supercomputers enables us to capture normal modes associated with the seismic point spectrum of a fully heterogeneous planet accurately. The computational cost can further be reduced using accelerating techniques.

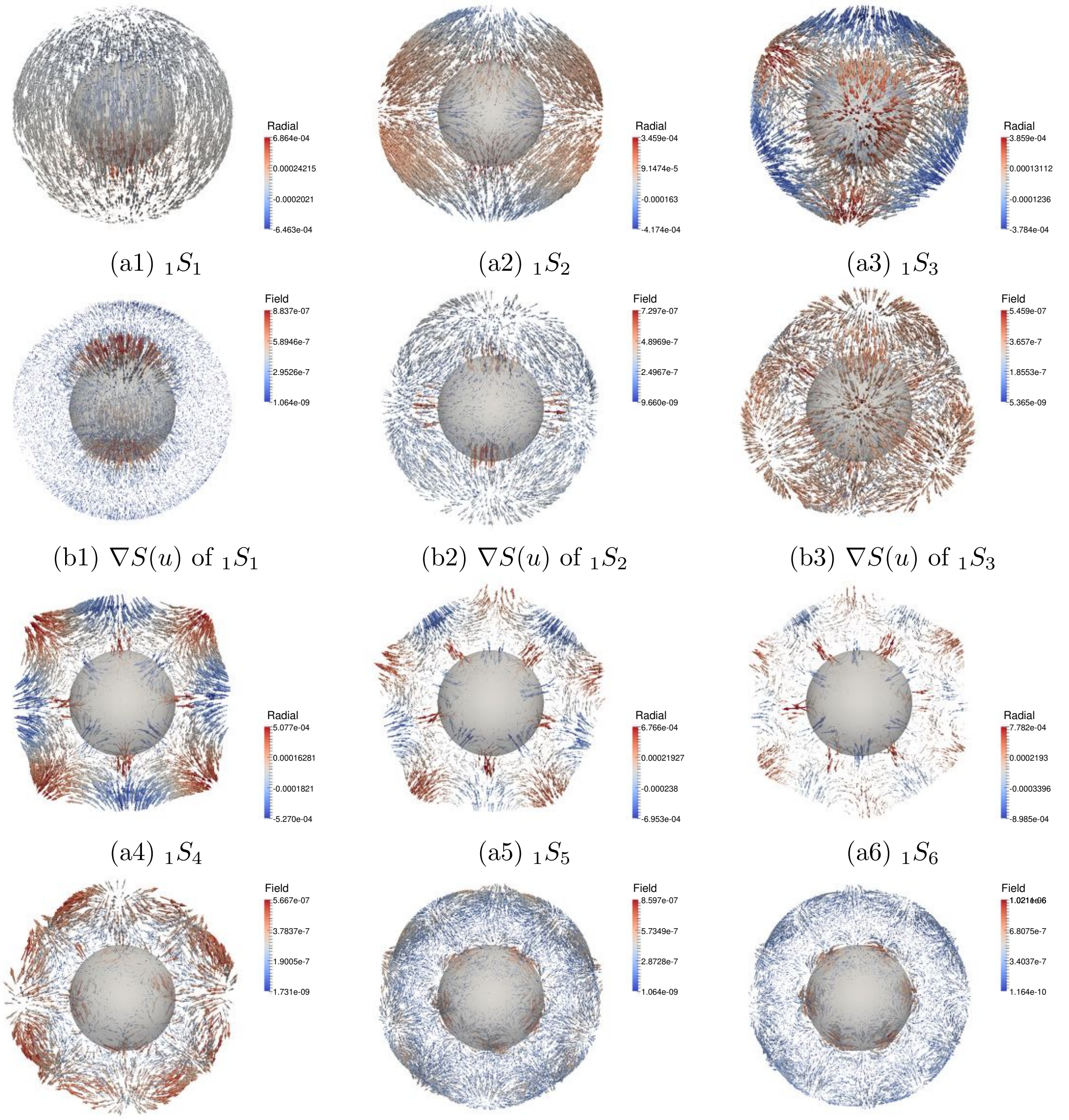

(a1) ${}_1S_1$ (a2) ${}_1S_2$ (a3) ${}_1S_3$

(b1) $\nabla S(u)$ of ${}_1S_1$ (b2) $\nabla S(u)$ of ${}_1S_2$ (b3) $\nabla S(u)$ of ${}_1S_3$

(a4) ${}_1S_4$ (a5) ${}_1S_5$ (a6) ${}_1S_6$

(b4) $\nabla S(u)$ of ${}_1S_4$ (b5) $\nabla S(u)$ of ${}_1S_5$ (b6) $\nabla S(u)$ of ${}_1S_6$

Figure 9. Visualization of ${}_1S_l$ branch of a Mars model with a three-dimensional crust and rotation from TM2Mp2 experiment. The light ball indicates the position of the core-mantle boundary. (a1)–(a6) present the modes ${}_1S_1$ to ${}_1S_6$, respectively. The unit in the color of (a1) - (a6) is meter. (b1)–(b6) present the perturbed gravitational field $\nabla S(u)$ of the modes ${}_1S_1$ to ${}_1S_6$, respectively. The unit in the colorbar of (b1)–(b6) is millimeter.

ACKNOWLEDGEMENT

This research was supported by the Simons Foundation under the MATH+X program, the National Science Foundation under grant DMS-1815143, the members of the Geo-Mathematical Imaging Group at Rice University, and XSEDE research allocation TG-EAR170019. J.S. would like to thank Petroleum Geo-Services for using their supercomputer

Abel. The work by R.L. was performed under the auspices of the U.S. Department of Energy by Lawrence Livermore National Laboratory under Contract DE-AC52-07NA27344 (LLNL-JRNL-xxxxxx). Y.X. and Y.S. were supported by NSF grants DMS-1521573, CCF-1505970 and CCF-1812695.

Disclaimer

REFERENCES

Akbarashrafi, F., Al-Attar, D., Deuss, A., Trampert, J., & Valentine, A., 2017. Exact free oscillation spectra, splitting functions and the resolvability of Earth's density structure, *Geophysical Journal International*, **213**(1), 58–76.

Al-Attar, D., Woodhouse, J. H., & Deuss, A., 2012. Calculation of normal mode spectra in laterally heterogeneous earth models using an iterative direct solution method, *Geophysical Journal International*, **189**(2), 1038–1046.

Allen, C. W., 1973. Astrophysical quantities.

Anderson, E., Bai, Z., Bischof, C., Blackford, S., Dongarra, J., Du Croz, J., Greenbaum, A., Hammarling, S., McKenney, A., & Sorensen, D., 1999. *LAPACK Users' guide*, vol. 9, SIAM.

Backus, G. & Gilbert, F., 1961. The rotational splitting of the free oscillations of the Earth, *Proceedings of the National Academy of Sciences of the United States of America*, **47**(3), 362.

Bai, Z. & Su, Y., 2005. SOAR: A second-order Arnoldi method for the solution of the quadratic eigenvalue problem, *SIAM Journal on Matrix Analysis and Applications*, **26**(3), 640–659.

Bai, Z., Demmel, J., Dongarra, J., Ruhe, A., & van der Vorst, H., 2000. *Templates for the solution of algebraic eigenvalue problems: a practical guide*, SIAM.

Banerdt, W., Smrekar, S., Lognonné, P., Spohn, T., Asmar, S., Banfield, D., Boschi, L., Christensen, U., Dehant, V., Folkner, W., et al., 2013. InSight: a discovery mission to explore the interior of Mars, in *Lunar and Planetary Science Conference*, vol. 44, p. 1915.

Belleguic, V., Lognonné, P., & Wieczorek, M., 2005. Constraints on the Martian lithosphere from gravity and topography data, *Journal of Geophysical Research: Planets*, **110**(E11).

Bills, B. G. & Ferrari, A. J., 1978. Mars topography harmonics and geophysical implications, *Journal of Geophysical Research: Solid Earth*, **83**(B7), 3497–3508.

Bissig, F., Khan, A., Van Driel, M., Stähler, S. C., Giardini, D., Panning, M., Drilleau, M., Lognonné, P., Gudkova, T. V., Zharkov, V. N., et al., 2018. On the detectability and use of normal modes for determining interior structure of Mars, *Space Science Reviews*, **214**(8), 114.

Chandrasekhar, S., 2013. *Hydrodynamic and hydromagnetic stability*, Oxford at the Claredon Press.

Clairaut, A. C., 1743. *Théorie de la figure de la terre, tirée des principes de l'hydrostatique*, chez David fils, libraire, ruë Saint-Jacques à la plume d'or.

Clinton, J. F., Giardini, D., Lognonné, P., Banerdt, B., van Driel, M., Drilleau, M., Murdoch, N., Panning, M., Garcia, R., Mimoun, D., et al., 2017. Preparing for InSight: An Invitation to Participate in a Blind Test for Martian Seismicity, *Seismological Research Letters*.

Dahlen, F., 1969. The normal modes of a rotating, elliptical earth—II Near-resonance multiplet coupling, *Geophysical Journal International*, **18**(4), 397–436.

Dahlen, F. & Sailor, R., 1979. Rotational and elliptical splitting of the free oscillations of the Earth, *Geophysical Journal International*, **58**(3), 609–623.

Dahlen, F. A., 1968. The normal modes of a rotating, elliptical Earth, *Geophysical Journal International*, **16**(4), 329–367.

Dahlen, F. A. & Tromp, J., 1998. *Theoretical global seismology*, Princeton University press.

de Hoop, M. V., Holman, S., & Pham, H., 2015. On the system of elastic-gravitational equations describing the oscillations of the earth, *arXiv preprint arXiv:1511.03200*.

de Hoop, M. V., Holman, S., Jimbo, S., & Nakamura, G., 2019. Characterization of the spectrum of the earth and normal modes, *in preparation*.

Deuss, A. & Woodhouse, J., 2004. Iteration method to determine the eigenvalues and eigenvectors of a target multiplet including full mode coupling, *Geophysical Journal International*, **159**(1), 326–332.

Deuss, A. & Woodhouse, J. H., 2001. Theoretical free-oscillation spectra: the importance of wide band coupling, *Geophysical Journal International*, **146**(3), 833–842.

Dollfus, A., 1972. New optical measurements of planetary diameters—Part IV: Planet Mars, *Icarus*, **17**(2), 525–539.

Dziewonski, A., Hales, A., & Lapwood, E., 1975. Parametrically simple earth models consistent with geophysical data, *Physics of the Earth and Planetary Interiors*, **10**(1), 12–48.

Dziewonski, A. M. & Anderson, D. L., 1981. Preliminary reference Earth model, *Physics of the earth and planetary interiors*, **25**(4), 297–356.

Fang, H. & Saad, Y., 2012. A Filtered Lanczos Procedure for Extreme and Interior Eigenvalue Problems, *SIAM Journal on Scientific Computing*, **34**(4), A2220–A2246.

Gilbert, F. & Dziewonski, A. M., 1975. An application of normal mode theory to the retrieval of structural parameters and source mechanisms from seismic spectra, *Philosophical Transactions of the Royal Society of London. Series A, Mathematical and Physical Sciences*, **278**(1280), 187–269.

Gimbutas, Z. & Greengard, L., 2011. FMMLIB3D 1.2, FORTRAN libraries for fast multiple method in three dimensions.

Goossens, S., Sabaka, T. J., Genova, A., Mazarico, E., Nicholas, J. B., & Neumann, G. A., 2017. Evidence for a low bulk crustal density for Mars from gravity and topography, *Geophysical research letters*, **44**(15), 7686–7694.

Greengard, L. & Rokhlin, V., 1997. A new version of the fast multipole method for the Laplace equation in three dimensions, *Acta numerica*, **6**, 229–269.

Greenspan, H. P. G., 1968. *The theory of rotating fluids*, Cambridge University Press.

Hara, T., Tsuboi, S., & Geller, R. J., 1991. Inversion for laterally heterogeneous earth structure using a laterally heterogeneous starting model: preliminary results, *Geophysical Journal International*, **104**(3), 523–540.

Hara, T., Tsuboi, S., & Geller, R. J., 1993. Inversion for laterally heterogeneous upper mantle S-wave velocity structure using iterative waveform inversion, *Geophysical Journal International*, **115**(3), 667–698.

Hoffnung, L., Li, R.-C., & Ye, Q., 2006. Krylov type subspace methods for matrix polynomials, *Linear Algebra and its Applications*, **415**(1), 52–81.

Holz, U. B., Golub, G. H., & Law, K. H., 2004. A subspace approximation method for the quadratic eigenvalue problem, *SIAM journal on matrix analysis and applications*, **26**(2), 498–521.

Irving, J. C., Cottaar, S., & Lekić, V., 2018. Seismically determined elastic parameters for Earth's outer core, *Science advances*, **4**(6), eaar2538.

Kennett, B. L., Engdahl, E., & Buland, R., 1995. Constraints on seismic velocities in the Earth from traveltimes, *Geophysical Journal International*, **122**(1), 108–124.

Khan, A., van Driel, M., Böse, M., Giardini, D., Ceylan, S., Yan, J., Clinton, J., Euchner, F., Lognonné, P., Murdoch, N., et al., 2016. Single-station and single-event marsquake location and inversion for structure using synthetic Martian waveforms, *Physics of the Earth and Planetary Interiors*, **258**, 28–42.

Kong, D., Zhang, K., & Schubert, G., 2010. Shapes of two-layer models of rotating planets, *Journal of Geophysical Research: Planets*, **115**(E12).

Li, R., Xi, Y., Vecharynski, E., Yang, C., & Saad, Y., 2016. A Thick-Restart Lanczos algorithm with polynomial filtering for Hermitian eigenvalue problems, *SIAM Journal on Scientific Computing*, **38**(4), A2512–A2534.

Lodders, K. & Fegley, B., 1998. *The planetary scientist's companion*, Oxford University Press on Demand.

Lognonné, P., 1991. Normal modes and seismograms in an anelastic rotating Earth, *Journal of Geophysical Research: Solid Earth*, **96**(B12), 20309–20319.

Lognonné, P., 2005. Planetary seismology, *Annu. Rev. Earth Planet. Sci.*, **33**, 571–604.

Lognonné, P. & Romanowicz, B., 1990. Modelling of coupled normal modes of the Earth: the spectral method, *Geophysical Journal International*, **102**(2), 365–395.

Lognonné, P., Banerdt, W. B., Giardini, D., Pike, W., Christensen, U., Laudet, P., De Raucourt, S., Zweifel, P., Calcutt, S., Bierwirth, M., et al., 2019. SEIS: Insight's seismic experiment for internal structure of Mars, *Space Science Reviews*, **215**(1), 12.

Masters, G., Barmine, M., & Kientz, S., 2011. Mineos: User Manual Version 1.0.2, *Cal Inst of Tech*.

Morelli, A. & Dziewonski, A. M., 1993. Body wave traveltimes and a spherically symmetric P-and S-wave velocity model, *Geophysical Journal International*, **112**(2), 178–194.

Nocedal, J. & Wright, S., 2006. *Numerical optimization*, Springer Science & Business Media.

Panning, M. P., Lognonné, P., Banerdt, W. B., Garcia, R., Golombek, M., Kedar, S., Knapmeyer-

Endrun, B., Mocquet, A., Teanby, N. A., Tromp, J., et al., 2017. Planned products of the Mars structure service for the InSight mission to Mars, *Space Science Reviews*, **211**(1-4), 611–650.

Park, J., 1986. Synthetic seismograms from coupled free oscillations: effects of lateral structure and rotation, *Journal of Geophysical Research: Solid Earth*, **91**(B6), 6441–6464.

Park, J., 1990. The subspace projection method for constructing coupled-mode synthetic seismograms, *Geophysical Journal International*, **101**(1), 111–123.

Park, J. & Gilbert, F., 1986. Coupled free oscillations of an aspherical, dissipative, rotating earth: Galerkin theory, *Journal of Geophysical Research: Solid Earth*, **91**(B7), 7241–7260.

Park, J., Song, T.-R. A., Tromp, J., Okal, E., Stein, S., Roult, G., Clevede, E., Laske, G., Kanamori, H., Davis, P., et al., 2005. Earth's free oscillations excited by the 26 December 2004 Sumatra-Andaman earthquake, *Science*, **308**(5725), 1139–1144.

Persson, P.-O. & Strang, G., 2004. A simple mesh generator in MATLAB, *SIAM review*, **46**(2), 329–345.

Radau, R., 1885. Sur la loi des densités à l'intérieur de la terre, *Academic Sciences (Paris) Comptes rendus, Tome C*, pp. 972–974.

Rivoldini, A., Van Hoolst, T., Verhoeven, O., Mocquet, A., & Dehant, V., 2011. Geodesy constraints on the interior structure and composition of mars, *Icarus*, **213**(2), 451–472.

Romanowicz, B., 1987. Multiplet-multiplet coupling due to lateral heterogeneity: asymptotic effects on the amplitude and frequency of the Earth's normal modes, *Geophysical Journal International*, **90**(1), 75–100.

Saad, Y., 2006. Filtered conjugate residual-type algorithms with applications, *SIAM Journal on Matrix Analysis and Applications*, **28**(3), 845–870.

Saad, Y., 2011. *Numerical methods for large eigenvalue problems: revised edition*, vol. 66, SIAM.

Shi, J., Li, R., Xi, Y., Saad, Y., & de Hoop, M. V., 2018. Computing planetary interior normal modes with a highly parallel polynomial filtering eigensolver, in *Proceedings of the International Conference for High Performance Computing, Networking, Storage, and Analysis, SC'18, Dallas, TX, USA, November 11-16, 2018*, pp. 71:1–71:13.

Shi, J., Li, R., Xi, Y., Saad, Y., & de Hoop, M. V., 2019. A Rayleigh-Ritz method based approach to computing seismic normal modes in the presence of an essential spectrum, *arXiv preprint arXiv:1906.11082*.

Si, H., 2015. TetGen, a Delaunay-based quality tetrahedral mesh generator, *ACM Transactions on Mathematical Software (TOMS)*, **41**(2), 11.

Sleijpen, G. L., Booten, A. G., Fokkema, D. R., & Van der Vorst, H. A., 1996a. Jacobi-Davidson type methods for generalized eigenproblems and polynomial eigenproblems, *BIT Numerical Mathematics*, **36**(3), 595–633.

Sleijpen, G. L., Van der Vorst, H. A., & Gijzen, M. v., 1996b. Quadratic eigenproblems are no problem, *SIAM News*, **29**(7), 8–9.

Slichter, L. B., 1961. The Fundamental free mode of the Earth's inner core, *Proceedings of the National Academy of Sciences*, **47**(2), 186–190.

Smith, D. E., Zuber, M. T., Solomon, S. C., Phillips, R. J., Head, J. W., Garvin, J. B., Banerdt, W. B., Muhleman, D. O., Pettengill, G. H., Neumann, G. A., et al., 1999. The global topography of Mars and implications for surface evolution, *Science*, **284**(5419), 1495–1503.

Tisseur, F. & Meerbergen, K., 2001. The quadratic eigenvalue problem, *SIAM review*, **43**(2), 235–286.

Um, J., Dahlen, F., & Park, J., 1991. Normal mode multiplet coupling along a dispersion branch, *Geophysical Journal International*, **106**(1), 11–35.

van Driel, M., Ceylan, S., Clinton, J. F., Giardini, D., Alemany, H., Allam, A., Ambrois, D., Balestra, J., Banerdt, B., Becker, D., et al., 2019. Preparing for InSight: Evaluation of the Blind Test for Martian Seismicity, *Seismological Research Letters*.

Weber, R. C., Lin, P.-Y., Garnero, E. J., Williams, Q., & Lognonne, P., 2011. Seismic detection of the lunar core, *science*, **331**(6015), 309–312.

Woodhouse, J., 1980. The coupling and attenuation of nearly resonant multiplets in the Earth's free oscillation spectrum, *Geophysical Journal International*, **61**(2), 261–283.

Woodhouse, J. & Dahlen, F., 1978. The effect of a general aspherical perturbation on the free oscillations of the Earth, *Geophysical Journal of the Royal Astronomical Society*, **53**(2), 335–354.

Woodhouse, J. & Deuss, A., 2007. Theory and observations – Earth's free oscillations, *Seismology and Structure of the Earth: Treatise on Geophysics*, **1**, 31–65.

Yang, H.-Y. & Tromp, J., 2015. Synthetic free-oscillation spectra: an appraisal of various mode-coupling methods, *Geophysical Journal International*, **203**(2), 1179–1192.

Ye, J., 2018. *Revisiting the computation of normal modes in SNREI models of planets – close eigenfrequencies*, Master's thesis, Rice University.

Yokota, R., 2013. An FMM based on dual tree traversal for many-core architectures, *Journal of Algorithms & Computational Technology*, **7**(3), 301–324.

Zhang, K. & Liao, X., 2017. *Theory and Modeling of Rotating Fluids: Convection, Inertial Waves and Precession*, Cambridge University Press.

Zuber, M. T., Smith, D., Solomon, S., Muhleman, D., Head, J., Garvin, J., Abshire, J., & Bufton, J., 1992. The Mars Observer laser altimeter investigation, *Journal of Geophysical Research: Planets*, **97**(E5), 7781–7797.

Zürn, W., Laske, G., Widmer-Schnidrig, R., & Gilbert, F., 2000. Observation of Coriolis coupled modes below 1 mHz, *Geophysical Journal International*, **143**(1), 113–118.

APPENDIX A: SHAPES OF A ROTATING PLANET

In this appendix, we revisit the derivation of Clairaut's equation in the context of condition (16) associated with the well-posedness and hydrostatic equilibrium (15).

A1 Derivation of Clairaut's equation

We start with the equation (15) in the co-rotating frame,

$$\nabla p = \rho^0 g' = -\rho^0 \nabla(\Phi^0 + \Psi),$$

where Φ^0, Ψ and g' are defined in (1), (3) and (4), respectively. Hence, transforming (3) into polar coordinates, the centrifugal potential takes form of

$$\Psi = \frac{\Omega^2 r^2}{3}[P_2(\cos\theta) - 1],$$

where $P_2(\cos\theta) = (3\cos^2\theta - 1)/2$ denotes the second-order Legendre polynomial. Equation (16) directly implies

$$\nabla\rho^0 \times g' = -\nabla\rho^0 \times \nabla(\Phi^0 + \Psi) = 0.$$

We now assume that the level sets of the density ρ^0 are spheroidal with mean radii, a, and ellipticities, $\epsilon(a)$. We note that the ellipticity will be a function of mean radius. The level sets can be written in polar coordinates as

$$r = r_a(\theta) = a\left[1 - \frac{2}{3}\epsilon(a)P_2(\cos\theta)\right].$$

Then

$$\rho^0(r_a(\theta), \theta) = \mathrm{const}_a =: \widehat{\rho}^0(a).$$

The density can be written as

$$\rho^0(r,\theta) = \sum_{n=0}^{\infty} \rho_n(r) P_n(\cos\theta),$$

where

$$\rho_n(r) = (n + 1/2)\int_0^{\pi} \widehat{\rho}^0(a) P_n(\cos\theta)\sin\theta\,\mathrm{d}\theta, \tag{A.1}$$

and $P_n(\cos\theta)$ denotes the Legendre polynomial. To first order in $|\epsilon|$, we have

$$a = r\left[1 + \frac{2}{3}\epsilon(r)P_2(\cos\theta)\right],$$

and substitute (A.1) into

$$\rho_n(r) = (n+1/2)\int_0^{\pi}\left[\widehat{\rho}^0(r) + \frac{2r}{3}\frac{\mathrm{d}\widehat{\rho}^0}{\mathrm{d}r}\epsilon(r)P_2(\cos\theta)\right]P_n(\cos\theta)\sin\theta\,\mathrm{d}\theta.$$

We note that

$$\rho_0(r) = \widehat{\rho}^0(r), \quad \rho_2(r) = \frac{2r}{3}\frac{\mathrm{d}\widehat{\rho}^0}{\mathrm{d}r}\epsilon(r),$$

with all of the other $\rho_n(r)$ zeros. To first order in $|\epsilon|$, we have

$$\rho^0(r,\theta) = \widehat{\rho}_0(r) + \frac{2r}{3}\frac{\mathrm{d}\widehat{\rho}^0}{\mathrm{d}r}\epsilon(r)P_2(\cos\theta),$$

With this density profile, we solve (1) in polar coordinates and obtain the expansion

$$\Phi^0(r,\theta) = \Phi_0(r) + \Phi_2(r)P_2(\cos\theta), \tag{A.2}$$

where

$$\begin{aligned}\Phi_0(r) &= -4\pi G\left[\frac{1}{r}\int_0^r \widehat{\rho}^0(r')r'^2\,\mathrm{d}r' + \int_r^{\infty}\widehat{\rho}^0(r')r'\,\mathrm{d}r'\right],\\ \Phi_2(r) &= -\frac{8\pi G}{15}\left[\frac{1}{r^3}\int_0^r \frac{\mathrm{d}\widehat{\rho}^0}{\mathrm{d}r'}r'^5\,\mathrm{d}r' + r^2\int_r^{\infty}\frac{\mathrm{d}\widehat{\rho}^0}{\mathrm{d}r'}\epsilon(r')\,\mathrm{d}r'\right].\end{aligned}$$

To first order in $|\epsilon|$, we obtain

$$\Phi^0(a,\theta) = \Phi_0'(a) + \Phi_2'(a)P_2(\cos\theta),$$

where

$$\begin{aligned}\Phi_a' &= -4\pi G\left[\frac{1}{a}\int_0^a \widehat{\rho}^0(a')a'^2\,\mathrm{d}a' + \int_a^{\infty}\widehat{\rho}^0(a')a'\,\mathrm{d}a'\right],\\ \Phi_2'(a) &= -\frac{8\pi G}{3}\left[\frac{\epsilon(a)}{a}\int_0^a \widehat{\rho}^0(a')a'^2\,\mathrm{d}a' - \frac{1}{5a^3}\int_0^a \widehat{\rho}^0(a')\,\mathrm{d}[\epsilon(a')(a'^5)] - \frac{a^2}{5}\int_a^{\infty}\widehat{\rho}(a')\,\mathrm{d}[\epsilon(a')]\right].\end{aligned}$$

To match the level sets of $\widehat{\rho}^0(a)$, to the same order in $|\epsilon|$ with (A.2), we simply must have the cancellation,

$$\Phi_2'(a) + \frac{\Omega^2 a^2}{3} = 0. \tag{A.3}$$

Equation (A.3) implies

$$\epsilon(a)a^2 \int_0^a \widehat{\rho}^0(a')a'^2 \,\mathrm{d}a' - \frac{1}{5}\int_0^a \widehat{\rho}^0(a')\,\mathrm{d}[\epsilon(a')(a'^5)] - \frac{a^5}{5}\int_a^\infty \widehat{\rho}(a')\,\mathrm{d}[\epsilon(a')] = \frac{\Omega^2 a^5}{8\pi G}.$$

Differentiating (A.3) with respect to a twice, we obtain

$$a^2\frac{\mathrm{d}^2\epsilon}{\mathrm{d}a^2} - 6\epsilon + \frac{6\widehat{\rho}^0}{\overline{\widehat{\rho}^0}}\left(a\frac{\mathrm{d}\epsilon}{\mathrm{d}a} + \epsilon\right) = 0, \tag{A.4}$$

where the average density

$$\overline{\widehat{\rho}^0}(a) = \frac{3}{a^3}\int_0^1 \widehat{\rho}^0(a')a'^2\,\mathrm{d}a' = \frac{3g_{(a)}}{4\pi G a}.$$

Equation (A.4) is exactly the Clairaut's equation (17). The derivation of the boundary conditions (cf. (18)) can be obtained from taking the limit of the differentiation of (A.3) with respect to a; see (Dahlen & Tromp 1998, (14.12)) for details. Clairaut's equation determines the ellipticities of the level sets. Through the hydrostatic equilibrium, we automatically guarantee that the level sets of p^0 coincide with the ones of the geopotential.

The Radau approximation (Radau 1885) is commonly used via introducing

$$\eta = \frac{a\,\mathrm{d}\epsilon}{\epsilon\,\mathrm{d}a}.$$

Substituting ϵ by η, we can rewrite (A.4) or (17)

$$\frac{\mathrm{d}}{\mathrm{d}a}\left(a^4 g_{(a)}\sqrt{1+\eta}\right) = 5g_{(a)}a^3 f(\eta), \tag{A.5}$$

where

$$f(\eta) = \frac{1+\eta/2-\eta^2/10}{\sqrt{1+\eta}}.$$

The range of the dimensionless independent variable is $\eta_{(0)} \leqslant \eta \leqslant \eta_{(r_e)}$, where

$$\eta_{(0)} = 0, \quad \eta_{(r_e)} = \frac{5\Omega^2 r_e^3}{2\epsilon_{(r_e)}GM^e} - 2.$$

Given a small ellipticity, $f(\eta)$ is quite close to one. Hence, the Radau's approximation is commonly made to replace (A.5) by

$$\frac{\mathrm{d}}{\mathrm{d}a}\left(a^4 g_{(a)}\sqrt{1+\eta}\right) \approx 5 g_{(a)} a^3.$$

We can then obtain the approximate solution of (17)

$$\epsilon(a) \approx \epsilon_{(r_e)} \exp\left(-\int_a^{r_e} \eta' a'^{-1}\,\mathrm{d}a'\right), \tag{A.6}$$

where

$$\epsilon_{(r_e)} = \frac{5\Omega^2 r_e^3}{2(\eta_{(r_e)}+2)GM^e} \approx \frac{10\Omega^2 r_e^3/GM^e}{4+25[1-3I^e/(M^e r_e^2)/2]^2}.$$

More details about hydrostatic ellipticity and Clairaut's equation can be found in (Dahlen & Tromp 1998, Chapter 14.1).

A2 More general density profiles

To overcome the limitation of ellipsoidal assumption, we model the density of the fully heterogeneous planet and the shape of the liquid core due to the effects of the centrifugal force. Since g' needs to be parallel to $\nabla\rho^0$, to find the satisfactory ρ^0 in (16), we form a related optimization

$$\min_\rho \mathcal{E}(\rho) = \frac{1}{2}\int_{\Omega^{\mathrm{F}}} \left[(g')^2(\nabla\rho)^2 - (g'\cdot\nabla\rho)^2\right]\,\mathrm{d}x + \frac{1}{2}\int_{\Sigma^{\mathrm{FS}}\cup\partial\tilde{X}^{\mathrm{F}}} \left[(g')^2\nu^2 - (g'\cdot\nu)^2\right]\,\mathrm{d}\Sigma, \tag{A.7}$$

subjects to constraints on conservation of mass,

$$\int_{\tilde{X}} \rho^0\,\mathrm{d}x = M^e, \tag{A.8}$$

and conservation of the moment of inertia,

$$\int_{\tilde{X}} |\Omega|^{-2}[\Omega^2 x^2 - (\Omega\cdot x)^2]\rho^0\,\mathrm{d}x = \int_{\tilde{X}} -2|\Omega|^{-2}\psi\rho^0\,\mathrm{d}x = I^e. \tag{A.9}$$

where M^e and I^e denote mass and moment of inertia, respectively; g' is a function of the density ρ. We note that g' depends on ρ^0 through Poisson's equation (cf. (1)) while we need to align the gradient of ρ^0 and g' at the same time.

We note that if ρ^* is a local solution,

$$\frac{\mathrm{d}}{\mathrm{d}\rho}\mathcal{E}(\rho^*) = 0. \tag{A.10}$$

where

$$\begin{aligned}\frac{\mathrm{d}}{\mathrm{d}\rho}\mathcal{E}(\rho)(\cdot) = \int_{\tilde{X}^{\mathrm{F}}} \left[\left(g' \cdot \frac{\mathrm{d}g'}{\mathrm{d}\rho}(\cdot)\right)(\nabla\rho)^2 + (g')^2\nabla\rho\cdot\nabla(\cdot)\right]\mathrm{d}x \\ - \int_{\tilde{X}^{\mathrm{F}}} \left[(g'\cdot\nabla\rho)\left(\frac{\mathrm{d}g'}{\mathrm{d}\rho}(\cdot)\cdot\nabla\rho + g'\cdot\nabla(\cdot)\right)\right]\mathrm{d}x \\ + \int_{\Sigma^{\mathrm{FS}}\cup\partial\tilde{X}^{\mathrm{F}}} \left[\left(g'\cdot\frac{\mathrm{d}g'}{\mathrm{d}\rho}(\cdot)\right)\nu^2 - (g'\cdot\nu)\left(\frac{\mathrm{d}g'}{\mathrm{d}\rho}(\cdot)\cdot\nu\right)\right]\mathrm{d}\Sigma.\end{aligned}$$

The combination of (A.8), (A.9) and (A.10) yields the Karush-Kuhn-Tucker conditions, or KKT conditions for short (Nocedal & Wright 2006). Given a perturbation $\delta\rho^*$ near ρ^* satisfies

$$\int_{\tilde{X}} \delta\rho^*\,\mathrm{d}x = 0, \quad \text{and} \quad \int_{\tilde{X}} -2|\Omega|^{-2}\psi\delta\rho^*\,\mathrm{d}x,$$

the fact that

$$\frac{\mathrm{d}}{\mathrm{d}\rho}\mathcal{E}(\rho^*)\delta\rho^* = 0,$$

implies that

$$g'(\rho^*)\times\nabla\rho^* = 0, \quad \text{and} \quad [g'(\rho^*)\times\nu]|_{\Sigma^{\mathrm{FS}}\cup\partial\tilde{X}^{\mathrm{F}}} = 0.$$

Equation (16) is then satisfied.